10

Dynamics of the Upper Mantle in Light of Seismic Anisotropy

Thorsten W. Becker[1,2] and Sergei Lebedev[3]

ABSTRACT

Seismic anisotropy records continental dynamics in the crust and convective deformation in the mantle. Deciphering this archive holds huge promise for our understanding of the thermo-chemical evolution of our planet, but doing so is complicated by incomplete imaging and non-unique interpretations. Here, we focus on the upper mantle and review seismological and laboratory constraints as well as geodynamic models of anisotropy within a dynamic framework. Mantle circulation models are able to explain the character and pattern of azimuthal anisotropy within and below oceanic plates at the largest scales. Using inferences based on such models provides key constraints on convection, including plate-mantle force transmission, the viscosity of the asthenosphere, and the net rotation of the lithosphere. Regionally, anisotropy can help further resolve smaller-scale convection, e.g., due to slabs and plumes in active tectonic settings. However, the story is more complex, particularly for continental lithosphere, and many systematic relationships remain to be established more firmly. More integrated approaches based on new laboratory experiments, consideration of a wide range of geological and geophysical constraints, as well as hypothesis-driven seismological inversions are required to advance to the next level.

10.1. INTRODUCTION

Anisotropy of upper mantle rocks records the history of mantle convection and can be inferred remotely from seismology. Seismic anisotropy refers to the orientational dependence of propagation velocities for waves traveling at different azimuths, or a difference in velocities for waves that are polarized in the horizontal or vertical plane such as Love and Rayleigh waves, respectively. "Anisotropy" without any qualifier shall here refer to the seismic kind caused by an anisotropic elastic stiffness tensor unless noted otherwise. Anisotropy is a common property of mineral assemblages and appears throughout the Earth, including in its upper mantle. There, anisotropy can arise due to the shear of rocks in mantle flow. As such, it provides a unique link between seismological observations and the evolution of our planet. However, given the need to resolve more parameters for an anisotropic than for an isotropic solid, seismological models for anisotropy are more uncertain, and the interpretation and link to flow necessarily non-unique.

Our personal views of seismic anisotropy have oscillated from a near-useless can of worms to the most useful constraint on convection ever, and we strive to present a more balanced view here. Anisotropy matters for all layers of the Earth, and there exist a number of excellent reviews covering the rock record, seismological observations, and laboratory constraints (e.g., Nicolas and

[1]*Institute for Geophysics, Jackson School of Geosciences, The University of Texas at Austin, Austin, USA*

[2]*Department of Geological Sciences, Jackson School of Geosciences, The University of Texas at Austin, Austin, TX, USA*

[3]*Dublin Institute for Advanced Studies, Dublin, Ireland*

Mantle Convection and Surface Expressions, Geophysical Monograph 263, First Edition.
Edited by Hauke Marquardt, Maxim Ballmer, Sanne Cottaar and Jasper Konter.

DOI: 10.1002/9781119528609.ch10

Christensen, 1987; Silver, 1996; Savage, 1999; Mainprice, 2007; Skemer and Hansen, 2016; Romanowicz and Wenk, 2017), as well as comprehensive treatments in textbooks (e.g., Anderson, 1989). Also, most of what was said in the overview of Long and Becker (2010) remains relevant. However, here we shall focus our discussion on the upper mantle within and underneath oceanic plates, the seemingly best understood part of mantle convection. We will highlight some of the insights afforded by seismic anisotropy within a convective context, and discuss selected open questions and how to possibly answer them.

10.2. OBSERVATIONS OF SEISMIC ANISOTROPY

A range of seismic observations show the presence of anisotropy in the Earth. In tomographic imaging of its three-dimensional distribution, anisotropy must normally be resolved simultaneously with the isotropic seismic velocity heterogeneity, typically greater in amplitude. Substantial non-uniqueness of the solutions for anisotropy can arise (e.g., Laske and Masters, 1998), and other sources of uncertainties include the treatment of the crust (e.g., Ferreira et al., 2010) and earthquake locations (Ma and Masters, 2015). In fact, the very existence of intrinsic anisotropy (e.g., due to lattice preferred orientation (LPO) of anisotropic mantle peridotite minerals) as opposed to apparent anisotropy (e.g., caused by layering of isotropic material of different wave speeds; e.g., Backus, 1962) has been debated (Fichtner et al., 2013; Wang et al., 2013).

At least regionally, the occurrence of anisotropy is, of course, not really in doubt since different lines of seismic evidence for it are corroborated by observations from mantle rocks (e.g., Ben Ismail and Mainprice, 1998; Mainprice, 2007). However, accurate determination of anisotropy is clearly not straightforward. Models based on data of different types, or even of the same type, are often difficult to reconcile and only agree on large spatial scales. Improvements in data sampling and anisotropy analysis methods are therefore subjects of active research, aimed at yielding more accurate and detailed information on the dynamics of the lithosphere and underlying mantle.

In order to ground the dynamics discussion, we first address the scales of resolution and distribution of seismic anisotropy coverage that are currently available to guide global mantle circulation assessment.

10.2.1. *Pn* Anisotropy

Historically, the detection of P wave anisotropy just below the Moho from refraction experiments in the Pacific Ocean was important in terms of establishing the existence of seismic anisotropy in the upper mantle and linking it to plate tectonics (e.g., Hess, 1964; Morris et al., 1969). It can be shown that the azimuth, φ, dependence of P wave speed anomalies, δv, for small seismic anisotropy at location $\mathbf{x}$ can be approximated by

$$\delta v(\varphi, \mathbf{x}) \approx A_0(\mathbf{x}) + A_1(\mathbf{x}) \cos(2\varphi) + A_2(\mathbf{x}) \sin(2\varphi) + A_3(\mathbf{x}) \cos(4\varphi) + A_4(\mathbf{x}) \sin(4\varphi) \quad (1)$$

(Backus, 1965). The simplest form of azimuthal anisotropy is due to the 2φ terms alone, and the corresponding 180° periodic pattern seen in Morris et al.'s (1969) results, for example (Figure 10.1). Based on such patterns, *Hess* (1964) concluded that the oceanic lithosphere and uppermost mantle must have undergone convective flow and made the connection to seafloor spreading (Vine and Matthews, 1963).

Anisotropy beneath continents was also detected, using both refraction and quarry-blast data (e.g., Bamford, 1977). More recently, *Pn* and *Sn* waves propagating from earthquakes have been used for mapping azimuthal anisotropy in the uppermost mantle, just beneath the Moho (e.g., Smith and Ekström, 1999; Buehler and Shearer, 2010), where they form a connection between shallow, crustal anisotropy and the deeper mantle observations such as from *SKS* splitting which we discuss next.

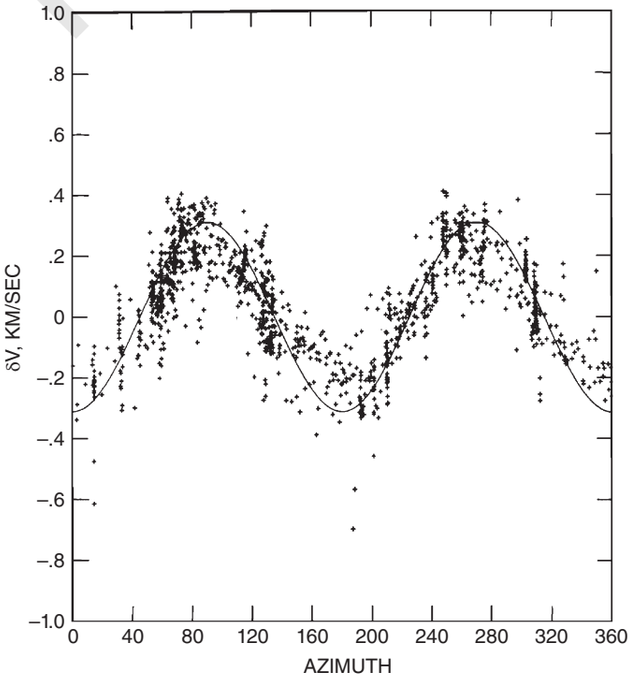

Figure 10.1 Velocity deviation for *Pn* from the mean (v_P = 8.159 km/s) in the central Pacific N and NW of Hawaii as a function of propagation azimuth along with a 2φ fit (eq. 1). Source: Modified from Morris et al. (1969).

10.2.2. Shear Wave Splitting

In the presence of azimuthal anisotropy, a shear wave pulse traveling into an anisotropic layer will be separated into two orthogonal pulses, one propagating within the medium's fast polarization plane (containing its "fast axis," or fast-propagation azimuth), and the other within the orthogonally oriented, slow propagation plane. At a seismic station, those split pulses will arrive separated by a delay time, δt, that is proportional to the integral of anisotropy strength and path length, assuming a uniform anisotropy orientation within the anisotropic layer (e.g., Silver and Chan, 1988; Vinnik et al., 1989). Such "splitting" is akin to optical birefringence and observed for local shear wave arrivals in the shallow crust ($\delta t \lesssim 0.2$ s) where it mainly reflects anisotropy due to aligned cracks, whose opening is controlled by tectonic stresses (Crampin and Chastin, 2003). For teleseismic shear waves, $\delta t \sim 1.2$ s, on average, and the splitting measurements can be related to whole-crustal and mantle anisotropy (Vinnik et al., 1992; Silver, 1996). *SKS* splitting due to anisotropic fabric within the crust is typically $\lesssim 0.3$ s, much smaller than that accumulated in the mantle. Areas with anomalously thick crust, for example Tibet, are the exception where crustal delay times have been estimated to be up to ~0.8 s (e.g., Agius and Lebedev, 2017).

The popular shear-wave splitting method yields a direct indication of anisotropy in the Earth (e.g., Savage, 1999). Outer-core-traversing waves such as *SKS* and *SKKS* are often used for the splitting measurements because they can yield information on receiver side anisotropy; source effects are excluded because of the *P* to *S* conversion upon exiting the core. The advantages of the method are its ease of use and its high lateral resolution. Figure 10.2 shows the current distribution of teleseismic shear wave splitting measurements with fairly dense sampling in most of the actively deforming continental regions.

The main disadvantage of *SKS* splitting is its poor vertical resolution; anisotropy may arise anywhere along the path. In the presence of one dominant anisotropic layer (say, the asthenosphere) with azimuthal anisotropy, the splitting parameters (delay times and fast azimuth) will characterize this layer directly. However, if multiple layers with different fast axes or more complex types of anisotropy are present, the net splitting will depend nonlinearly on backazimuth and the depth-variable anisotropy (e.g., Silver and Savage, 1994; Rümpker and Silver, 1998; Saltzer et al., 2000). Resolving some of the depth-dependence is possible with dense spatial coverage but requires long station deployment times and good back-azimuthal sampling (e.g., Chevrot et al., 2004; Long et al., 2008; Abt and Fischer, 2008; Monteiller and Chevrot, 2011).

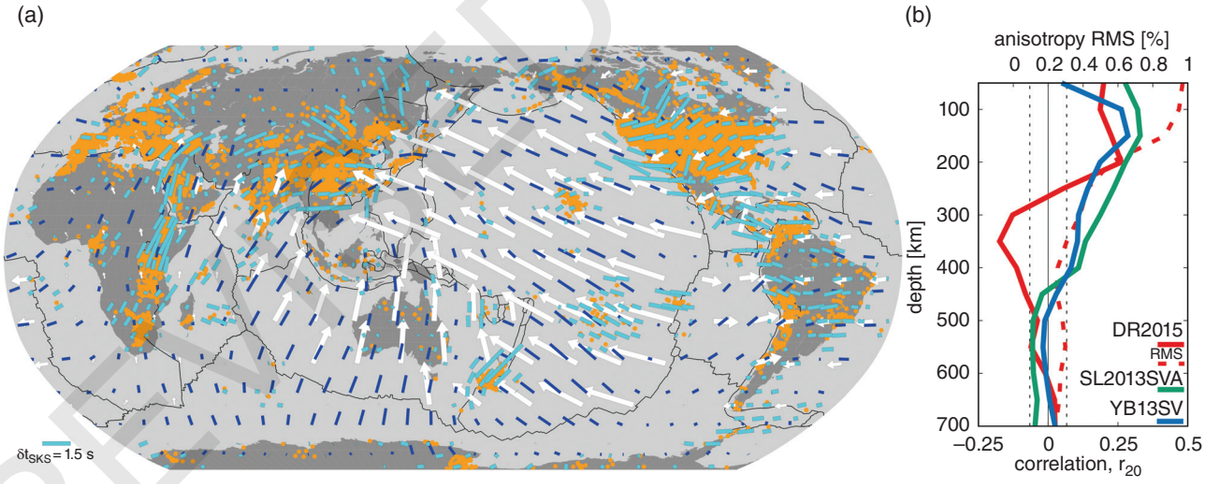

Figure 10.2 Azimuthal anisotropy of the upper mantle. (a) Non-zero *SKS* splitting observations (orange dots) fit using spherical harmonics up to degree, $\ell = 20$ (cyan sticks, processed as in *Becker et al.* 2012, and updated as of 01/2019), and compared to the global azimuthal anisotropy model SL2013SVA at 200 km depth (blue sticks; Schaeffer et al. 2016), and MORVEL (DeMets et al., 2010) plate motions in a spreading-aligned reference frame (white vectors; *Becker et al.* 2015). (b) Correlation up to $\ell = 20$, r_{20} (solid lines), between *SKS* splitting (a) and three seismological models: DR2015 (Debayle and Ricard, 2013, RMS anisotropy also shown with dashed line), SL2013SVA (Schaeffer et al. 2016), and YB13SV (Yuan and Beghein, 2013). Dashed vertical lines are 95% significance levels for r_{20} (cf. Becker et al., 2007a, 2012; Yuan and Beghein, 2013). Source: (a) Becker et al. (2012), Schaeffer et al. (2016), Becker et al. (2016), DeMets et al. (2010), Becker et al. (2015). (b) Debayle and Ricard (2013), Schaeffer et al. (2016), Yuan and Beghein (2013), Becker et al. (2007a).

When considering the uncertainty in the mantle depths where teleseismic splitting arises, we can focus on high stress/low temperature boundary layers where dislocation creep might dominate (Karato, 1992; Gaherty and Jordan, 1995; McNamara et al., 2001). For *SKS* splitting, this means uncertainty on whether the delay times are caused by anisotropy in the lithosphere, asthenosphere, the transition zone between the upper and lower mantle (e.g., Fouch and Fischer, 1996; Wookey and Kendall, 2004), and/or the core-mantle boundary/D" region (reviewed elsewhere in this volume).

The integrated anisotropy of the lithosphere alone is typically not enough to fully explain *SKS* splitting delay times (e.g., Vinnik et al., 1992; Silver, 1996). Comparisons between local and teleseismic splitting from subduction zones are usually consistent with an origin of most *SKS* splitting observations within the top ~400 km of the mantle (e.g., Fischer and Wiens, 1996; Long and van der Hilst, 2006). Together with surface wave models of anisotropy (Figure 10.2b) as well as mineral physics and dynamics considerations discussed below, this suggests a dominant asthenospheric cause of *SKS* splitting.

10.2.3. Surface Waves

There are a range of other approaches used for mapping anisotropy, including study of *P*- wave polarization (Schulte-Pelkum et al., 2001), body-wave imaging (e.g., Plomerová et al., 1996; Ishise and Oda, 2005; Wang and Zhao, 2008), receiver-function anisotropy analysis (e.g., Kosarev et al., 1984; Farra and Vinnik, 2002; Schulte-Pelkum and Mahan, 2014), and normal-mode measurements (e.g., Anderson and Dziewoński, 1982; Beghein et al., 2008). However, for global-scale imaging of the upper mantle, surface wave analysis holds the most promise for making the link to depth-dependent convection scenarios.

Just as the response of the Earth to a seismic event can be expressed as a superposition of normal modes (standing waves), it can be decomposed into a sum of surface waves (traveling waves; Dahlen and Tromp, 1998). The depth sensitivity of surface waves depends on their period; the longer the period, the deeper the sample. Global maps of surface-wave phase velocities at periods from ~35–150 s, sampling the mantle lithosphere and asthenosphere have been available for over two decades (e.g., Ekström et al., 1997; Trampert and Woodhouse, 2003). More recently, global models have been constructed with surface waves in broadening period ranges, up to ~25–250 s (Ekström, 2011) and even up to 10–400 s (Schaeffer and Lebedev, 2013), although at the shortest of the periods the event-station measurements can no longer cover the entire globe.

Using the ambient noise wave field, speeds of the surface waves excited by ocean waves are routinely measured in a 1–35 s period range, i.e., sensing from the uppermost crust to the uppermost mantle (Shapiro et al., 2005; Bensen et al., 2007; Ekström et al., 2009). Anthropogenic noise yields measurements at frequencies of a few Hz to a few tens of Hz, sampling within the shallowest, sedimentary layers (Mordret et al., 2013). Cross-correlations of seismograms from teleseismic earthquakes yield phase-velocity measurements down to periods as short as 5–10 s, sampling the upper and middle crust (Meier et al., 2004; Adam and Lebedev, 2012) (Figure 10.3) and up to periods over 300 s (e.g., Lebedev et al., 2006), sampling the deep upper mantle and transition zone.

Rayleigh waves are mainly sensitive to vertically polarized shear wave speed, v_{SV}, with smaller, although non-negligible, sensitivity to horizontally polarized shear wave velocity, v_{SH}, and v_P (e.g., Montagner and Nataf, 1986; Romanowicz and Snieder, 1988; Dahlen and Tromp, 1998). The azimuthal expansion of eq. 1 holds for surface waves as well (Smith and Dahlen, 1973), and in the olivine dominated upper mantle, the 2φ terms of eq. 1 are expected to be the main signature of azimuthal anisotropy for Rayleigh waves (Montagner and Nataf, 1986; Montagner and Anderson, 1989, cf. Figure 10.3). At the same periods, Love waves are mainly sensitive to v_{SH} at shallower depths, and the 4φ terms of azimuthal anisotropy, depending on assumptions about petrology (Montagner and Nataf, 1986).

Radial anisotropy (the difference between v_{SV} and v_{SH}) was documented based on the finding that Love and Rayleigh waves could not be fit simultaneously by the same Earth model (Anderson, 1961; Aki and Kaminuma, 1963; McEvilly, 1964). Azimuthal anisotropy of surface waves was also established early (Forsyth, 1975), and Montagner and Tanimoto (1991) presented an integrated model of upper mantle anisotropy capturing both radial and azimuthal contributions.

A full description of seismic anisotropy is achieved by an elastic stiffness tensor with 21 independent components instead of the isotropic two (e.g., Anderson, 1989), but often hexagonal symmetry (or "transverse isotropy") is assumed. In this case, five parameters fully specify the tensor, for example the vertically and horizontally polarized *S* and *P* wave speeds, v_{SV}, v_{SH}, v_{PV}, and v_{PH}, respectively, and a parameter η, which determines how waves polarized between the horizontal and vertical plane transition from v_{SH} to v_{SV} (e.g., Dziewoński and Anderson, 1981; Kawakatsu, 2016). In the case of radial anisotropy imaging, the hexagonal symmetry axis is assumed vertical, and $\xi = (v_{SH}/v_{SV})^2$ is commonly used as a measure of anisotropy strength. For the case of azimuthal anisotropy, the hexagonal symmetry axis is in the horizontal plane and its azimuth determines the 2φ terms of eq. (1), e.g., for

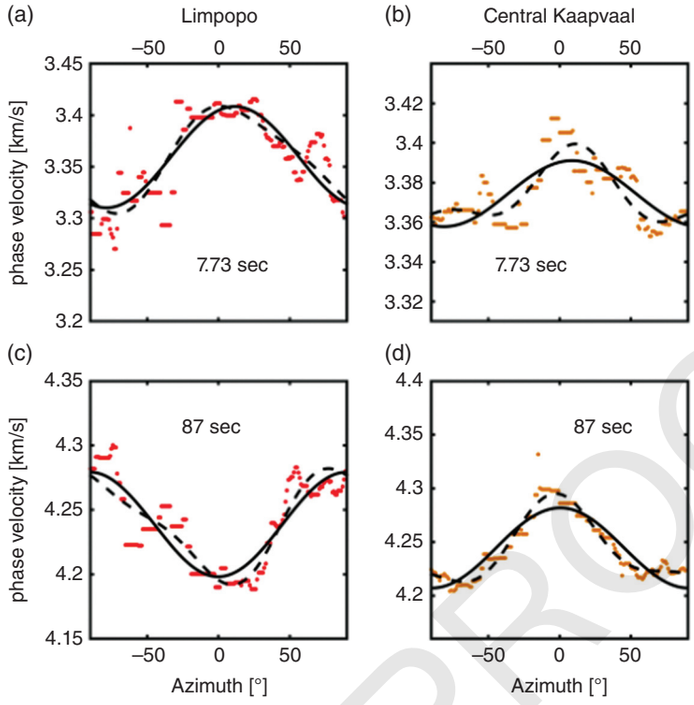

Figure 10.3 Azimuth, φ, dependent anisotropy of Rayleigh-wave phase velocities in different regions (a and c vs. b and d) in southern Africa. Rayleigh waves at the 7.73 s period (a and b) sample primarily the upper and middle crust, and at 87 s (c and d), the lower part of the cratonic lithosphere, respectively. Dots show the phase-velocity measurements, binned and smoothed with a 30° sliding window. Solid black lines: best-fitting models with isotropic and 2φ terms (see eq. 1). Dashed black lines: best-fitting models with isotropic, 2φ, and 4φ terms. Source: Modified from *Ravenna* (2018), using measurements from Adam and Lebedev (2012).

the Rayleigh wave, v_{SV}, anisotropy or the fast axes of *SKS* splitting.

The construction of large waveform datasets over the last two decades has enabled increasingly detailed surface-wave tomography of upper-mantle anisotropy on global scales. A number of 3-D radial (e.g., Nataf et al., 1984; Ekström and Dziewoński, 1998; Panning and Romanowicz, 2006; Kustowski et al., 2008; French and Romanowicz, 2014; Auer et al., 2014; Moulik and Ekström, 2014; Chang et al., 2015) and azimuthal (e.g., Tanimoto and Anderson, 1984; Montagner, 2002; Debayle and Ricard, 2013; Yuan and Beghein, 2013; Schaeffer et al., 2016) (Figure 10.2) anisotropy models have been presented.

Many features of anisotropic structure are now consistently mapped for the upper mantle on continent scales. The mutual agreement of different anisotropy models, however, remains well below that of models of isotropic heterogeneity (Becker et al., 2007a; Auer et al., 2014; Chang et al., 2015; Schaeffer et al., 2016). Given the typical period range for fundamental mode surface wave measurements, both radial and azimuthal anisotropy are best constrained in the uppermost ~350 km of the mantle, even though comprehensive waveform analysis (e.g., Lebedev et al., 2005; Priestley et al., 2006; Panning and Romanowicz, 2006) or the explicit use of overtones (e.g., Trampert and van Heijst, 2002; Beghein and Trampert, 2004) extends the depth range to the bottom of the transition zone (~700 km) and beyond, at least theoretically.

Dense arrays of seismic stations enable higher lateral resolution surface wave anisotropy imaging regionally (e.g., Shapiro et al., 2004; Deschamps et al., 2008a; Lin et al., 2011; Takeo et al., 2018; Lin et al., 2016). On those scales, it is also easier to explore uncertainties, and probabilistic 1-D profiles obtained with Monte Carlo inversion schemes can be used, for example, to explore the trade-off between the radial and azimuthal anisotropy layer imaging (e.g., Beghein and Trampert, 2004; Agius and Lebedev, 2014; Bodin et al., 2016; Ravenna et al., 2018).

Uncertainties aside, array measurements can present unambiguous evidence of anisotropy in the crust and upper mantle beneath the array footprint. Figure 10.3 shows an example for a continental plate site. The

measurements of phase velocities for different period Rayleigh waves clearly indicate seismic azimuthal anisotropy of the 2φ kind (cf. Figure 10.1), and a change in the fast propagation azimuth from the shallow to the deeper layers.

10.3. INTERPRETATION OF SEISMIC ANISOTROPY

10.3.1. Origin of Upper Mantle Anisotropy

Shear due to convective flow is expected to lead to the formation of lattice (or, more appropriately, "crystallographic") preferred orientation anisotropy in the olivine-dominated upper mantle, meaning that anisotropy should be a record of mantle flow (e.g., McKenzie, 1979; Tanimoto and Anderson, 1984; Ribe, 1989). The foundations for this common assumption include the observation that natural xenolith and exhumed mantle massif samples show such alignment (e.g., Nicolas and Christensen, 1987; Ben Ismail and Mainprice, 1998), and that laboratory experiments indicate a link between the orientation and amount of shear induced deformation and the resulting LPO (e.g., Karato et al., 2008; Skemer and Hansen, 2016). For olivine single crystals ~75% of the total elastic anisotropy is hexagonal, while most of the remainder is of orthorhombic symmetry (e.g., Browaeys and Chevrot, 2004). For assemblages, the hexagonal contribution ranges from ~80% for peridotites from spreading centers to ~55% in xenoliths from kimberlites in the compilation of Ben Ismail and Mainprice (1998). This apparent predominance of hexagonal anisotropy for mantle assemblages motivates the approximations usually made in seismology.

LPO development is usually assumed to require not just solid state convection but deformation within the dislocation creep regime. For typical olivine grain sizes of order mm, this implies that LPO formation and hence seismic anisotropy will be enhanced in the mantle's boundary layers (e.g., Karato, 1998; Podolefsky et al., 2004; Becker, 2006). Thus, shear within the asthenosphere underneath the lithospheric plates, say within the top ~400 km of the mantle, is expected to dominate the upper mantle signal of geologically recent anisotropy formation. The more slowly deforming lithosphere may record past episodes of deformation or creation in the case of continental and oceanic lithosphere, respectively (e.g., Vinnik et al., 1992; Silver, 1996).

There are possible other contribution to anisotropy besides LPO due to past and present mantle flow, such as preserved shape preferred fabrics or LPO within the crust (e.g., Godfrey et al., 2000; Brownlee et al., 2017), or the effects of partial melt (e.g., Blackman et al., 1996; Holtzman and Kendall, 2010; Hansen et al., 2016a). An effectively anisotropic partial-melt layer at the base of the lithosphere can explain observed impedance contrasts, for example (e.g., Kawakatsu et al., 2009). However, it is commonly held that regions of large partial melt fraction are of limited spatial extent away from spreading centers and continental rifts. This will be revisited below.

When deforming olivine aggregates in the laboratory, anisotropy strength due to LPO saturates at linear strains, γ, of $\lesssim 5\ldots10$ (e.g., Zhang and Karato, 1995; Bystricky et al., 2000; Hansen et al., 2014). Preexisting textures likely require larger strain values for reorientation, in broad accordance with observations from the field (e.g., Skemer and Hansen, 2016). For strain-rates that might be typical for the asthenosphere, say $\sim 5 \times 10^{-15}$ s^{-1} (e.g., a plate moving at 5 cm/yr inducing shear over a ~300 km thick layer), $\gamma = 5$ is achieved in ~30 Myr. Using circulation computations and finite strain tracking, one arrives at similar numbers; times of advection in mantle flow are commonly between 10 and 30 Myr over path lengths between 500 km to 1500 km, respectively (Becker et al., 2006a). In the highly deforming asthenosphere, these relatively short saturation or reworking times of order of 10s of Myr then determine the "memory" of seismic anisotropy, i.e., how much convective history and changes in plate motions are recorded. Within the cold and hence slowly deforming lithosphere, older episodes of deformation may be partially frozen-in for very long times, say $\gtrsim$300 Myr in continents. This is longer than the characteristic lifetime of an oceanic plate, though it is most likely not a continuous record that is being preserved (e.g., Silver, 1996; Boneh et al., 2017).

In strongly and coherently deforming regions of the upper mantle, we therefore expect that the amplitude of anisotropy is mainly governed by the orientation of olivine LPO near saturation. Exceptions include spreading centers and subduction zones where a transition from simple to pure shear during vertical mass transport will lead to strong reworking of fabrics (e.g., Blackman and Kendall, 2002; Kaminski and Ribe, 2002; Becker et al., 2006a). Such reworking is where different mineral physics approaches regrettably diverge in their predictions (e.g., Castelnau et al., 2009), and constraints from the lab and field indicate a mismatch with widely used LPO modeling approaches (Skemer et al., 2012; Boneh et al., 2015).

Irrespective of the details of the LPO formation mechanism, we note that anisotropy strength is not expected to scale with absolute plate or slab velocity, rather it is spatial variations in velocities (i.e. strain-rates) that control the rate of anisotropy saturation. Any relationship between plate speed and the signature of anisotropy is thus likely indirect, for example such that LPO formation under plate-motion induced shear is more efficient

compared to other processes like small-scale convection for faster plates with higher strain-rates (van Hunen and Čadek, 2009; Husson et al., 2015).

10.3.2. Anisotropy and Plate Motions

Given the link between LPO induced anisotropy and mantle flow, a firstorder constraint on convection can thus be provided by the existence of significant radial anisotropy in the upper mantle (e.g., Dziewoński and Anderson, 1981; Nataf et al., 1986; Beghein et al., 2006; Wang et al., 2013). Due to the alignment of the fast symmetry axis of an LPO aggregate in the vertical or horizontal direction, a simple mantle convection cell with an oceanic plate forming at its top limb should display $v_{SH} > v_{SV}$ within and below the plate's interiors (dominating the global average), and $v_{SV} > v_{SH}$ within the up- and downwelling limbs underneath spreading centers and subduction zones, respectively (e.g., Montagner and Guillot, 2000).

Relatively few studies have addressed the distribution of average radial anisotropy in light of mantle dynamics (e.g., Regan and Anderson, 1984; Montagner and Tanimoto, 1991; Chastel et al., 1993; Montagner, 1994; Babuška et al., 1998; Plomerová et al., 2002; Gung et al., 2003). Both average and broad-scale patterns of radial anisotropy can be shown to be consistent with the predictions from mantle convection computations with dislocation/diffusion creep olivine rheologies at grain sizes of order mm (Becker et al., 2008; Behn et al., 2009). Amplitudes of radial anisotropy appear underpredicted within the lithosphere by convective LPO models, particularly within continental regions (Becker et al., 2008). This hints at an additional contribution, e.g., due to frozen in anisotropy similar to what has been suggested for oceanic plates (e.g., Beghein et al., 2014; Auer et al., 2015).

We now proceed to discuss the large-scale origin of azimuthal seismic anisotropy (Figure 10.2) in light of oceanic plate boundary dynamics (cf. Montagner and Guillot, 2000). Within the low-strain-rate lithosphere, we expect azimuthal anisotropy to record past deformation during creation of the plate. This deformation may be inferred from the spreading directions and rates that are recorded in the gradients of seafloor age (e.g., Conrad and Lithgow-Bertelloni, 2007). We can then compare the fast axes with paleo-spreading orientations (e.g., Hess, 1964; Forsyth, 1975; Nishimura and Forsyth, 1989).

Figure 10.4a shows a typical result for such a comparison. Spreading orientations overall represent a good first-order model of azimuthal anisotropy in the lithosphere. They appear recorded more clearly in anisotropy in younger rather than in older seafloor, particularly in the Pacific plate (e.g., Smith et al., 2004; Debayle and Ricard, 2013; Becker et al., 2014), perhaps due to small-scale reheating at ages older than ~80 Ma (cf. Nagihara et al., 1996; Ritzwoller et al., 2004). Seafloor that was generated during higher spreading rate activity shows smaller orientational misfits with lithospheric azimuthal

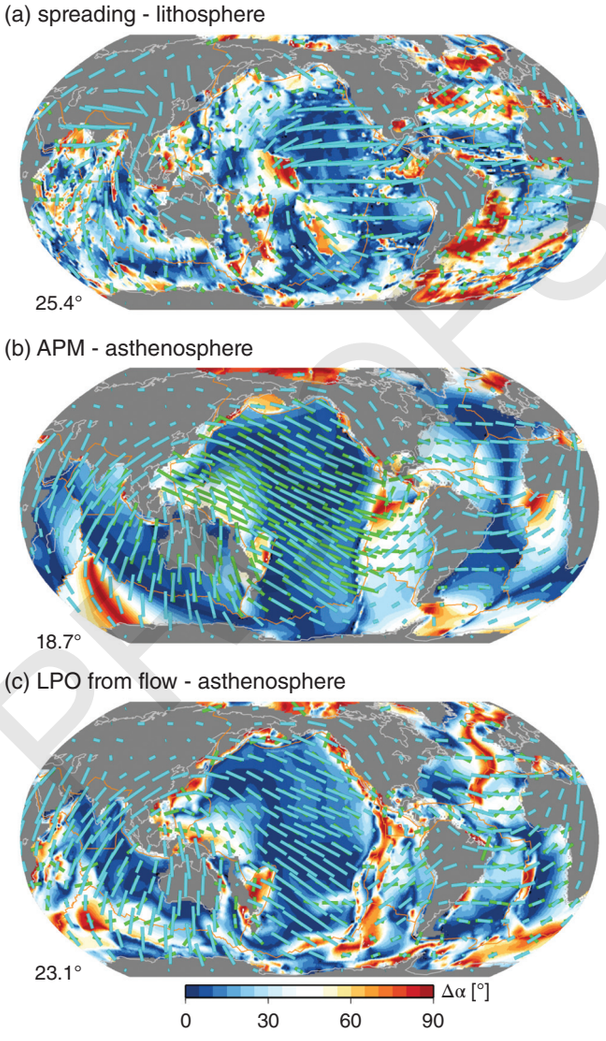

Figure 10.4 Angular orientational misfit, $\Delta\alpha$, in the oceanic plate regions, computed between azimuthal anisotropy from SL2013SA (cyan sticks; Schaeffer et al., 2016) and geodynamic models (green). (a) Seismology at 50 km depth vs. paleo-spreading orientations inferred from seafloor age gradients. (b) SL2013SA at 200 km depth vs. absolute plate motions in the spreading-aligned reference frame (Becker et al., 2015). (c) SL2013SA at 200 km depth vs. synthetic anisotropy based on LPO formed in mantle flow (model of Becker et al., 2008). Numbers in lower left indicate average angular misfit in the oceanic regions. See Becker et al. (2014) for more detail on the analysis. Source: (a) Schaeffer et al., 2016. (b) Becker et al., 2015. (c) Becker et al., (2008). Becker et al., (2014).

anisotropy than regions that were generated by slower spreading (Becker et al., 2014), possibly indicating variations in the degree of ductile to brittle deformation (Gaherty et al., 2004), asymmetry or non-ridge-perpendicular orientation of slow spreading, or the relative importance of small-scale convection (e.g., van Hunen and Čadek, 2009).

Besides controlling factors such as spreading rate and seafloor age which may have general relevance for the creation of oceanic lithosphere, there are also geographic differences (Figure 10.4a); the Atlantic displays larger misfits than the Pacific, for example. This might be an overall reflection of tectonics (Atlantic spreading rates are slower than Pacific ones). However, the resolution of surface wave anisotropy imaging is also spatially variable (e.g., Laske and Masters, 1998; Becker et al., 2003) and in particular earthquake source location errors are mapped into larger variations in fast azimuths in the Atlantic than the Pacific domain (Ma and Masters, 2015).

If we seek an explanation for deeper, asthenospheric, layers, we can consider the orientation of azimuthal anisotropy compared to plate motions. The underlying assumption for such comparisons is that the direction of surface velocities in some absolute reference frame, e.g., as based on hotspots (e.g., Minster and Jordan, 1978) are indicative of the orientation of shear due to motion of the lithosphere with respect to a relatively stationary deep mantle. This is called an absolute plate motion (APM) model.

Even in the absence of convective contributions due to density anomalies, plate-induced mantle flow can lead to regionally significant deviations from the shear deformation that is indicated by the APM model. This is true in terms of the velocity magnitude, i.e. if the plate is leading the mantle or vice versa in simple shear (Couette) type flow (with possible effects on anisotropy dip angle), and it is also important in that the orientation of mantle flow may be very different from that of plate motion (Hager and O'Connell, 1981). The sense of asthenospheric shear may thus be at large angles to APM orientations. Moreover, the degree to which asthenospheric flow is of the plug (Poiseuille) type matters because the depth distribution of strain-rates will be different for each case (Natarov and Conrad, 2012; Becker, 2017; Semple and Lenardic, 2018). These effects are likely most relevant for slowly moving plates.

Setting aside these complexities, the comparison between APM and azimuthal anisotropy in the asthenosphere can provide some guidance as to how much of the pattern of anisotropy might be related to convection and, importantly, it does not require any further modeling assumptions. Comparisons with APM have thus been used extensively to explore how anisotropy might be related to mantle flow (e.g., Montagner and Tanimoto, 1991; Debayle and Ricard, 2013).

Figure 10.4b shows such a comparison of azimuthal anisotropy with APM orientations at nominally 200 km depth. Much of the patterns of azimuthal anisotropy in the oceanic regions can be matched by APM alignment, indicating a relationship between flow-induced LPO and seismological constraints. The global oceanic misfit is smaller than for the lithospheric match to paleo-spreading, at average angular misfit $\lesssim 20^{\circ}$. This is of the order of orientational uncertainties for surface wave studies for azimuthal anisotropy (e.g., Laske and Masters, 1998; Becker et al., 2003; Ma and Masters, 2015; Schaeffer et al., 2016). In this sense, the APM model, its inherently non-physical nature notwithstanding, provides a plausible explanation for asthenospheric anisotropy and confirms that plates are an integral part of mantle convection.

However, there appear to be systematic geographic variations in misfit in the APM asthenospheric match of Figure 10.4b whose origin is unclear. Moreover, any use of crustal kinematics in an absolute sense, of course, requires a choice of reference frame. Figure 10.4b uses the spreading-aligned reference frame, which was argued by Becker et al. (2015) to provide a parsimonious explanation to a range of constraints for geologically recent plate dynamics. This reference frame is similar to hotspot reference frames with relatively small net rotation of the lithosphere with respect to the deep mantle (e.g., Ricard et al., 1991; Becker, 2006; Conrad and Behn, 2010).

10.3.3. Mantle Circulation Modeling

If we seek to make use of our understanding of the physics of mantle circulation instead of comparing anisotropy to APM, we need to approximate the details of mantle flow and LPO formation. In particular, we need to make choices as to how to infer density anomalies and viscosity variations within the mantle. In fact, comparisons of azimuthal anisotropy with the seminal mantle circulation model of Hager and O'Connell (1981) followed soon after (Tanimoto and Anderson, 1984).

To arrive at estimates of mantle flow, typically slab structure from seismicity (Hager, 1984) or isotropic seismic tomography is scaled to temperature using simplified approximations to what would be inferred from mineral physics and assumptions as to mantle composition (e.g., Hager et al., 1985). Such circulation model predictions can, for example, explain geoid anomalies as long as there is an increase in viscosity toward the lower mantle (e.g., Richards and Hager, 1984; King and Masters, 1992), and the associated mantle tractions also provide a powerful explanation for the patterns and rates of plate motions (e.g., Ricard and Vigny, 1989; Forte et al., 1991; Lithgow-Bertelloni and Richards, 1998; Becker and O'Connell, 2001). However, mantle velocities are strongly dependent on the variable force transmission that results from lateral

viscosity variations (e.g., Conrad and Lithgow-Bertelloni, 2002; Becker, 2006; van Summeren et al., 2012; Alisic et al., 2012), and those will affect strain rates and hence anisotropy development. In the case of seismic anisotropy, we can thus ask if geodynamic models of mantle flow that are constructed based on other constraints (e.g., geoid or plate motions) also fit seismic anisotropy, and we can use anisotropy to further refine such models.

Assuming that velocities of mantle flow are estimated, we need to make the link to seismic anisotropy. This can be done by simply examining shear in a certain layer of the mantle (i.e. velocity differences; e.g., Tanimoto and Anderson, 1984), computing the finite strain ellipsoid (FSE) accumulated along a particle path (e.g., McKenzie, 1979; Ribe, 1989), or estimating LPO using more complex micro-physical models (e.g., Ribe and Yu, 1991; Wenk and Tomé, 1999; Tommasi, 1998; Kaminski and Ribe, 2001; Blackman et al., 2002). Such approaches have the capability to incorporate laboratory results that indicate the importance of recrystallization during LPO anisotropy formation under sustained shear (e.g., Zhang and Karato, 1995; Bystricky et al., 2000). Experiments also suggest that olivine slip system strength and hence the type of LPO being formed depends on deformation conditions and volatile content (e.g., Jung and Karato, 2001; Katayama et al., 2004).

The most common, A-type LPO regime (Karato et al., 2008; Mainprice, 2007) appears most prevalent among xenolith and mantle massif samples (Ben Ismail and Mainprice, 1998; Bernard et al., 2019). The corresponding modeled LPO predictions of best-fit hexagonal symmetry axis alignment in flow are broadly consistent with the orientation of the longest FSE axis. Exceptions are regions of strong fabric reworking such as underneath spreading centers or other complex flow scenarios (Ribe and Yu, 1991; Blackman et al., 2002; Kaminski and Ribe, 2002; Becker et al., 2006a; Conrad et al., 2007). Other approximations of the LPO such as the infinite strain axis (Kaminski and Ribe, 2002) appear to perform less well in comparisons with surface wave based anisotropy than LPO estimates (Becker et al., 2014). These tests indicate that anisotropy from mantle flow may perhaps be best modeled either by using the FSE (equivalent to whisker orientation in analog experiments; Buttles and Olson, 1998) or by computing bulk-approximate (Goulding et al., 2015; Hansen et al., 2016b) or grain-oriented (e.g., Kaminski et al., 2004; Castelnau et al., 2009) descriptions of actual LPO formation, on which we will focus here.

Once LPO is estimated for olivine or olivine-orthopyroxene assemblages by some scheme (e.g., Kaminski et al., 2004), we then need to assign elastic tensors to each virtual grain to compute effective anisotropy. Choices as to the pressure and temperature dependence of elasticity tensor components as well as the averaging scheme have noticeable effects (Becker et al., 2006a; Mainprice, 2007), but are likely smaller than uncertainties in seismological imaging on global scales.

Given dramatic improvements in seismological constraints during the 20 years after the fundamental comparison of Tanimoto and Anderson (1984), a number of groups revisited mantle circulation modeling in light of azimuthal anisotropy ~15 years ago. Gaboret et al. (2003) and Becker et al. (2003) focused on Pacific and global-scale surface wave models, respectively, while Behn et al. (2004) and Conrad et al. (2007) explored matching *SKS* splitting in oceanic plate regions and globally. These models usually find that moving from APM models to mantle flow computations that respect the return flow effects caused by plate motions alone does not improve, or sometimes rather significantly degrades, the fit to seismologically inferred anisotropy. The added physical realism of estimating flow and LPO does come into play once density anomalies are considered for the flow computations, and such models typically outperform APM approaches (Gaboret et al., 2003; Becker et al., 2003; Behn et al., 2004; Conrad et al., 2007; Conrad and Behn, 2010; Becker et al., 2014).

Figure 10.4c shows an example of how LPO formed under dislocation creep in a global circulation model that includes density anomalies (as used in Becker et al., 2008, to study radial anisotropy) matches azimuthal anisotropy (Schaeffer et al., 2016) at asthenospheric depths. While the average misfit for the LPO model is larger than for the comparison with APM (Figure 10.4b), the regions of large misfit appear now more easily associated with tectonic processes. In particular, large misfits are found underneath spreading centers, where LPO is expected to be reworked (e.g., Blackman and Kendall, 2002; Kaminski and Ribe, 2002), a process that is as of yet fairly poorly constrained experimentally (Skemer et al., 2012; Hansen et al., 2014, 2016b). In the models, a consequence of this reworking is that elastic anisotropy locally displays slow axis hexagonal symmetry as well as significant non-hexagonal contributions in regions with pure shear type of flow (Becker et al., 2006a). Besides, non-LPO contributions due to partial melting is expected to matter close to the spreading centers (Blackman et al., 1996; Blackman and Kendall, 1997; Holtzman and Kendall, 2010; Hansen et al., 2016a). However, given that regions of large misfit appear confined to "special" places and that all oceanic basins otherwise fit quite well (Figure 10.4c), we consider the match of LPO predictions from mantle flow and anisotropy a first-order achievement of "applied geodynamics" (Gaboret et al., 2003; Becker et al., 2003; Behn et al., 2004; Conrad et al., 2007).

The LPO model of Figure 10.4c relies on the approach of Becker et al. (2006a) who computed fabrics using the

method of Kaminski et al. (2004) along particle paths. Tracers are first followed back in time until, upon iteration, their advective forward paths accumulate a critical finite strain, γ_c, at each observational point. The idea is that any existing textures will be overprinted, and in the case of the example in Figure 10.4c, $\gamma_c \approx 6$. This choice leads to a good match to radial anisotropy averages and patterns (Becker et al., 2008) as well as regional *SKS* splitting delay times (e.g., Becker et al., 2006b; Miller and Becker, 2012), and is consistent with overprinting strains from field and laboratory deformation (Skemer and Hansen, 2016).

Assuming that the LPO that is predicted from mantle flow modeling provides at least a statistically appropriate estimate of anisotropy in the upper mantle, we can then use geodynamic models to revisit the hexagonal approximation of seismological imaging. Globally, ~80% of LPO anisotropy is found to be of hexagonal character on average; within regional anomalies, the orthorhombic contribution can reach $\lesssim 40\%$ (Becker et al., 2006a). This is close to the orthorhombic fraction (~45%) invoked by the subducted asthenosphere model of Song and Kawakatsu (2012). However, on global scales, geodynamic models confirm that the simplifying assumption of hexagonal anisotropy made by seismology appear justified if olivine LPO is the major source of anisotropy in the upper mantle.

The flow computation used in Figure 10.4c assumes that mantle circulation is stationary over the timescales needed to achieve γ_c. This is a potentially questionable approximation, and time-evolving scenarios expectedly produce larger complexity of LPO predictions, e.g., compared to steady-state subduction scenarios (Buttles and Olson, 1998; Faccenda and Capitanio, 2013; Zhou et al., 2018). However, reconstructing the time-evolution of convective flow introduces additional uncertainties due to having to use plate reconstructions and the nonreversibility of the energy equation (e.g., Steinberger and O'Connell, 1997; Conrad and Gurnis, 2003). More to the point, Becker et al. (2003) found that the improvements in terms of the match of anisotropy predictions when allowing for time-dependent mantle circulation were ambiguous. Preliminary tests with newer models confirm that asthenospheric anisotropy predictions are not affected much compared to steady-state approximations as in Figure 10.5c, as expected given the relatively short advective times. However, the shallower regions within the lithosphere appear somewhat sensitive to which plate reconstruction is used. This provides an avenue for further research.

Boundary Layer Anisotropy. One of the major achievements of geodynamics is to have linked the bathymetry and heatflow of oceanic seafloor to the half-space cooling of a convective thermal boundary layer (Turcotte and Oxburgh, 1967; Parsons and Sclater, 1977). Shear in the region below the mechanical boundary layer that is contained within the thermal lithosphere should determine LPO formation (Podolefsky et al., 2004). This is indeed seen when considering the amplitude of azimuthal

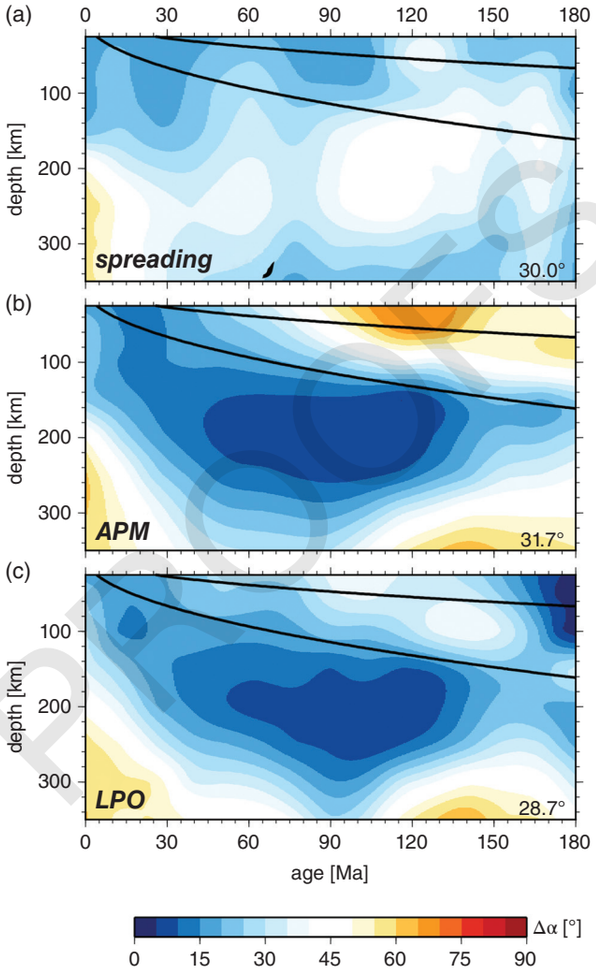

Figure 10.5 (a) Angular orientational misfit, $\Delta\alpha$, underneath the Pacific plate, computed between fast propagation orientations from SL2013SA (Schaeffer et al., 2016) and paleo-spreading orientations, as a function of depth and seafloor age bins (cf. Figure 10.4a). Black lines are 600°C and 1200°C isotherms from half-space cooling, respectively. (b) Angular misfit between azimuthal anisotropy and absolute plate motions in the spreading-aligned reference frame (Becker et al. 2015). (c) Angular misfit between azimuthal anisotropy and synthetics based on computing LPO formation in global mantle flow (model of Becker et al. 2008). Numbers in lower right indicate average angular misfit for each panel. See Becker et al. (2014) for more detail. Source: (a) (Schaeffer et al. 2016). (b) Becker et al. 2015. (c) Becker et al. (2014).

anisotropy as a function of seafloor age (e.g., Burgos et al., 2014; Beghein et al., 2014) though alignment with APM is perhaps a better measure as anisotropy orientations should be better constrained than amplitudes (Debayle and Ricard, 2013).

Figure 10.5 shows a typical result where the misfit of the three geodynamic models of Figure 10.4 is shown for the Pacific plate as a function of age. As noted, paleospreading is only a good model for the shallowest oceanic lithosphere and relatively young ages. However, alignment with APM or LPO provides a good explanation of azimuthal anisotropy within a 150–200 km thick layer below the ~1200°C isotherm (cf. Burgos et al., 2014; Beghein et al., 2014), as expected given the depth distribution of deformation within the dislocation creep regime (Becker et al., 2008; Behn et al., 2009). Alignment with both LPO and APM underneath the cold isotherm breaks down at ages older than ~150 Ma (cf. Figures 8.4b and 8.4c), perhaps a reflection of small-scale convection (van Hunen and Čadek, 2009).

Comparison of geodynamic predictions with different seismological models leads to similar conclusions (Becker et al., 2014). However, radial anisotropy does not appear to follow half-space cooling (Burgos et al., 2014), and those discrepancies will be revisited below. The approach of computing mantle circulation and then inferring LPO anisotropy from it to constrain convection, of course, translates to the bottom boundary layer of the mantle as well (Romanowicz and Wenk, 2017), and a separate chapter in this volume is dedicated to this problem.

10.3.4. Examples of Inferences That Extend Beyond the Reference Model

As the previous section illustrates, we can indeed use azimuthal seismic anisotropy as a constraint for mantle rheology and upper mantle convection, and in particular arrive at a consistent and quantitative, first-order description of lithosphere-asthenosphere dynamics underneath oceanic plates. The formation of olivine LPO within the "typical" A type slip system under convective flow and plates forming according to half-space cooling appears to provide a globally appropriate geodynamic reference model, and seismic anisotropy is another constraint for plate formation. We should keep in mind the relative success of this "reference" model (e.g., Figures 8.4 and 8.5) as we move on to briefly discuss some of the more indirect inferences based on seismic anisotropy, and in particular when we conclude by discussing regional or process level complications.

Mantle flow is driven by density anomalies and modulated by viscosity, and in theory both of these can be inverted for using seismic anisotropy assuming it is formed by the shear due to spatial variations in velocity. In practice, additional constraints are needed for all but the simplest tests. One important question in mantle dynamics is that of the appropriate reference frame for surface motions with respect to the lower mantle. Different reference frames yield a range of estimates for trench advance or rollback, for example (e.g., Chase, 1978; Funiciello et al., 2008) with implications for regional tectonics and orogeny.

Given that seismic anisotropy due to LPO is formed under the shear that corresponds to the motion of the surface relative to the stagnant lower mantle, one may thus postulate that the best APM is that which minimizes the misfit to anisotropy. This was addressed by Kreemer (2009) based on *SKS* splitting and explored by Montagner and Anderson (2015) for surface waves and individual plate motions with focus on the Pacific. The spreading-aligned reference of Figure 10.4b naturally minimizes the misfit with a number of surface-wave based estimates of azimuthal anisotropy, and their individual best-fit poles are very similar. This implies that the anisotropy-constrained reference frame may have general relevance, with implications for the relative strength of transform faults, for example (Becker et al., 2015).

One can also use mantle circulation modeling to explore the depth-distribution of the shear that corresponds to different degrees of net rotation of the lithosphere (Zhong, 2001; Becker, 2006), and then test how such a shear component would affect the match of global circulations models to seismic anisotropy. This exploits the fact that the match to anisotropy is sensitive to where in the mantle shear is localized (Becker et al., 2003; Conrad and Behn, 2010). Becker (2008) used the match to surface wave based azimuthal anisotropy to argue that net rotation should be less than $\lesssim$ 0.2°/Myr. Conrad and Behn (2010) considered both *SKS* splitting and surface wave anisotropy and further explored this "speed limit" on net rotation. They find a permissible net rotation of ~0.25°/Myr for an asthenospheric viscosity that is one order of magnitude smaller than that of the upper mantle.

Using models that self-consistently generate plate motions, Becker (2017) showed that anisotropy constraints on asthenospheric viscosity are consistent across different modern azimuthal anisotropy models, and that even slab-driven flow alone leads to perturbations of the large-scale match of LPO anisotropy from flow that is seen in Figure 10.4c. A moderate sub-oceanic viscosity reduction to ~0.01…0.1 times the upper mantle viscosity is strongly preferred by both the model match to azimuthal anisotropy and the fit to plate motions (Figure 10.6), even though there exists a typical trade-off with layer thickness (Richards and Lenardic, 2018). In particular, suggested high partial melt, lubricating zones underneath oceanic plates (e.g., Kawakatsu et al., 2009; Schmerr, 2012) appear to not be widespread enough

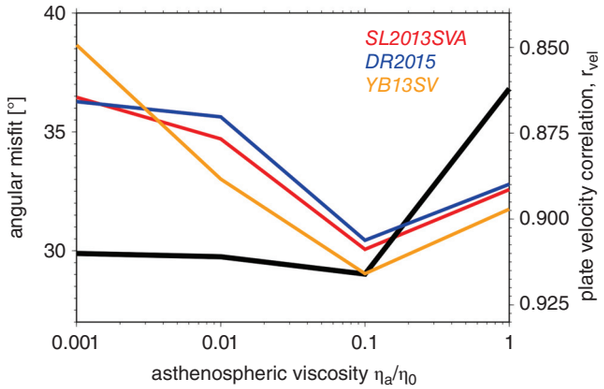

Figure 10.6 Angular misfit (minimum with depth) between flow model predictions and azimuthal seismic anisotropy for oceanic domain for three different seismological models: SL2013SVA (Schaeffer et al., 2016, as in Figure 10.4), DR2015 (Debayle and Ricard, 2013), and YB13SV (Yuan and Beghein, 2013) (colored lines), and misfit of predicted plate velocities (black line), as a function of asthenospheric viscosity reduction for a 300 km thick layer. Source: Modified from Becker (2017), see there for detail.

to affect largescale mantle shear, or else it should be seen in the match to seismic anisotropy (Becker, 2017).

On a regional scale, *SKS* splitting provides better lateral resolution than traditional surface wave analyses and is thus widely used to infer the role of mantle flow for tectonics, particularly within continental plates (Figure 10.2). When combined with flow models, we can exploit the sensitivity of mantle circulation to density anomalies and viscosity variations (e.g., Fouch et al., 2000; Hall et al., 2000; Behn et al., 2004; Becker et al., 2006b). This was done by Miller and Becker (2012) in a quasi-inverse sense, exploring a large number of global mantle flow computations with a range of density and viscosity models to test which (in particular with respect to continental keel geometry and strength) are consistent with *SKS* splitting in NE South America. A similar approach was used on a larger-scale for South America by Hu et al. (2017), and Faccenna et al. (2013) to infer a low viscosity channel underneath the Red Sea, for example.

Another possible approach to explore the effects of mantle convection, helpful in the absence of good isotropic tomography for example, is to test different forward models of the effect of density anomalies, e.g., compared to plate-scale flow for plumes (e.g., Walker et al., 2005; Ito et al., 2014) or details of subduction and delamination scenarios (e.g., Zandt and Humphreys, 2008; Alpert et al., 2013). In such regional contexts, mantle flow models provide the capability to explore the impact of depth variations in seismic anisotropy, as those are ideally recorded in the back-azimuthal dependence of *SKS* splitting (e.g., Blackman and Kendall, 2002; Hall et al., 2000; Becker et al., 2006b). Subduction zone *SKS* splitting anisotropy is, however, complex to the extent that the correct background model becomes questionable (e.g., Long, 2013), as discussed in a different chapter of this volume.

A question to ask whenever seismic anisotropy observations are used to infer mantle dynamics is how consistent any model is with a range of observations besides the anisotropy data, e.g., in terms of the geoid, dynamic topography, or plate motions. Some studies invoke different effects that may impact mantle flow (e.g., a small-scale plume, inherited structure in the lithosphere, volatile variations in the asthenosphere) for nearly every single different *SKS* split, often without any consistent flow modeling, and so trivially explain all data perfectly in the extreme case. Other studies, such as the approach illustrated in Figure 10.4c, strive for a broad-scale match to the observations, within an actual geodynamic framework that respects continuum mechanics conservation laws. This can then invite further study as to which effects (e.g., intraplate deformation, volatile variations of frozen in structure) may be required regionally on top of the reference model. Clearly, there is a continuum between those quasi end-members.

10.4. OPEN QUESTIONS

10.4.1. Regional Complexities and Scale-Dependent Resolution

Navigating between the extremes of a possibly very complicated model or simulation that matches all data, and a simple model which may or may not be a good reference given large regional misfits is, of course, not an uncommon challenge in the Earth sciences. However, the complexities of anisotropy, both in terms of spatially variable resolution and in terms of possible mechanisms for anisotropy generation, seem to make these trade-offs more acute for efforts of linking anisotropy to mantle flow.

Oceanic Plates Revisited. The previous discussion of convection dynamics as seen by seismic anisotropy focused on large spatial scales and seismic models that are derived from global surface wave datasets. *SKS* splitting for oceanic island stations (Figure 10.2) are also usually well fit by the density-driven mantle circulation models (e.g., Behn et al., 2004; Conrad et al., 2007). Increasingly, we can interpret results from ocean bottom seismometer deployments, which slowly infill the oceanic plates in terms of high-resolution and high-quality regional constraints (e.g., Isse et al., 2019). In particular,

deployments that are designed to image "normal" or at least "melt free" oceanic plates are very valuable to further develop the thermo-mechanical reference model of plate generation that was alluded to previously (e.g., Lin et al., 2016; Takeo et al., 2018; Kawakatsu and Utada, 2017; Russell et al., 2019).

Alas, the regional results are often at odds with inferences from global models, particularly when it comes to the variation in strength of radial and azimuthal anisotropy with depth. This has long been debated and results are sensitive to the dataset selection and applied corrections (e.g., Ferreira et al., 2010; Ekström, 2011; Rychert and Harmon, 2017). For presumably typical oceanic lithosphere, there is evidence for radial anisotropy with $v_{SH} > v_{SV}$ in the lithosphere (e.g., Gaherty et al., 1996; Russell et al., 2019), but regional (Takeo et al., 2013) and many global models show a deeper peak in radial anisotropy (~80…150 km, e.g., Nettles and Dziewoński, 2008; French and Romanowicz, 2014; Auer et al., 2014; Moulik and Ekström, 2014). The latter would be more consistent with a geologically recent, convective LPO origin of radial anisotropy.

Moreover, while azimuthal anisotropy strength appears to follow half-space cooling similar to the region of low angular misfit in Figure 10.5, radial anisotropy appears to have limited seafloor age dependence (Burgos et al., 2014; Beghein et al., 2014; Auer et al., 2015; Isse et al., 2019). This might indicate that LPOs due to spreading and/or petrological heterogeneities (e.g., Kawakatsu et al., 2009; Schmerr, 2012; Sakamaki et al., 2013; Ohira et al., 2017) are frozen in during the generation of plates (e.g., Beghein et al., 2014; Auer et al., 2015; Russell et al., 2019), or that the effects of meltinduced LPO mask the age dependence that would be expected (Hansen et al., 2016a).

At least some mid-lithospheric structure appears required for oceanic plates that is unrelated to simple LPO anisotropy (Rychert and Harmon, 2017), perhaps indicating a mid-lithospheric discontinuity similar to what has been discussed for continental plates (e.g., Yuan and Romanowicz, 2010; Selway et al., 2015). However, the mechanical effects of the lithospheric component of convection in terms of asthenospheric shear appear to be captured by half-space cooling and azimuthal anisotropy as reflected in Figure 10.5 (Becker et al., 2014).

Anisotropy in Continents. Referring to his analysis of *P* wave seismic anisotropy in oceanic plates, Hess (1964) noted that "the structure and history of the whole ocean floor can probably be worked out much more rapidly than the more complicated land surface of the Earth," and this has been very much true. Thermal mantle convection explains the motions of the nearly rigid oceanic plates well, but the distributed and protracted deformation record of the continental lithosphere is strongly affected by rheological and compositional effects, and still presents many questions.

One way to explore the consistency between different ways of imaging anisotropy is to consider the match between *SKS* splitting estimates and surface wave based azimuthal anisotropy in continents where *SKS* splits are preferentially measured, because of station logistics (Figure 10.2). Montagner et al. (2000) conducted such a comparison using an approximate method and found that agreement in terms of the fast azimuth pattern was limited. A more positive assessment with a more complete *SKS* dataset was provided by Wüstefeld et al. (2009) who found a match at the longest wavelengths. Becker et al. (2012) revisited this comparison and showed that full waveform modeling of *SKS* splitting leads to only moderate differences in the apparent splitting compared to averaging for the current generation of global surface models. Indeed, the agreement in terms of fast azimuths is limited when *SKS* splits are smoothed over less than ~2000 km length scales. This does at least partly reflecting the inherent resolution limits of global models (e.g., Debayle and Ricard, 2013; Schaeffer et al., 2016). Most surface wave models also underpredict *SKS* delay times, likely because of the required regularization (cf. Schaeffer et al., 2016).

Figure 10.2b shows that the long-wavelength correlation between *SKS* fast axis patterns and different surface wave models is best in the upper ~400 km of the mantle, where azimuthal anisotropy models show the largest power and are most in agreement with each other (Becker et al., 2012; Yuan and Beghein, 2013). This finding is consistent with a common origin, the suggested dominance of an uppermost mantle, asthenospheric anisotropy to typical *SKS* splitting results (e.g., Fischer and Wiens, 1996; Silver, 1996), and an LPO induced by mantle flow origin (Figure 10.5; e.g., Becker et al., 2008, 2014). Figure 10.2b also indicates a hint of a drop in correlation in the lithosphere, and regionally, it is clear that there is both depth-dependence in the surface-wave imaged anisotropy and the match with *SKS* splitting (e.g., Deschamps et al., 2008b; Yuan et al., 2011; Lin et al., 2016; Takeo et al., 2018).

Such discrepancies motivate an alternative approach that exploits the difference in depth sensitivity between *SKS* and Rayleigh waves (Marone and Romanowicz, 2007; Yuan and Romanowicz, 2010). One can use surface waves to constrain the shallow part of a model, say above ~250 km, and then use the complementary resolution of the path component of teleseismic waves beneath that region to exploit *SKS* constraints on anisotropy. Along with constraints from radial anisotropy (e.g., Gung et al., 2003) and alignment of 2φ anisotropy with APM motions, such models have been used to infer a thermochemically layered structure of the North American

craton (Yuan and Romanowicz, 2010; Yuan et al., 2011), for example.

Given the now more complete coverage of the continental US with *SKS* splitting thanks to USArray (Figure 10.2a), we recently revisited the question of agreement between surface wave models and *SKS*, and found that *SKS* remain poorly matched even by newer surface wave models. An exception is the model of Yuan et al. (2011) for most of North America, but that model attempts to fit *SKS* splits by design. This implies that the depth resolution of large-scale surface wave models is, on a continent-scale, not at the level where details in possible anisotropic layering could be consistently determined, particularly below ~200 km (Yuan et al., 2011).

10.4.2. Uncertainties About Microphysics

Formation of Olivine LPO. There is now a range of experimental work that documents how olivine develops LPO under shear. Among the modern studies, Zhang and Karato (1995) and the large-strain experiments of Bystricky et al. (2000) showed how olivine *a*-axes cluster within the shear plane for the common, A type fabric, or the high-stress D type. A-type LPO is found most commonly in natural samples (Ben Ismail and Mainprice, 1998; Bernard et al., 2019), and provides the most straightforward link between anisotropy and flow as was explored in section 3.3.

However, Jung and Karato (2001) and Katayama et al. (2004) found that additional LPO types can develop depending on deviatoric stress, temperature, and water content conditions, and mineral physics modeling approaches can reproduce those fabrics by assigning different relative strength to the major olivine slip systems (Kaminski, 2002; Becker et al., 2008). The predictions for anisotropy can be markedly different from A: The B (high-water, high-stress/low-temperature type) would lead us to expect azimuthal anisotropy to be oriented perpendicular to shear, and this might explain some of the subduction zone complexities, though likely not all trench-parallel splitting (Kneller et al., 2005; Lassak et al., 2006). Effective B types are also seen in high partial-melt experiments (Holtzman et al., 2003). The C (high-water, low-stress/high-temperature) type is expressed such that $v_{SV} > v_{SH}$ under horizontal shear, implying a complete reorientation of the relationship between flow and radial anisotropy (Karato et al., 2008; Becker et al., 2008).

At present, it is not entirely clear how olivine LPO formation depends on deformation conditions, in particular in conjunction with ambient pressure (Karato et al., 2008). For example, Ohuchi et al. (2012) substantiated a transition from A→B LPO as a function of water content at low confining pressures. However, Ohuchi and Irifune (2013) showed that the dependence on volatile content appears reversed at higher pressures (below ~200 km depth), such that A would be the high-volatile content LPO, and changes in LPO, perhaps mainly depth-dependent (cf. Mainprice et al., 2005; Jung et al., 2009).

If we consider the range of natural xenolith and ophiolite samples, all of the LPO types documented in the lab are indeed found in global compilations (Mainprice, 2007; Bernard et al., 2019). However, samples from individual sites show a range of different LPOs, at presumably similar deformation conditions in terms of volatile content and deviatoric stress. Moreover, when such conditions are estimated from the samples, no clear systematics akin to the laboratory-derived phase diagrams arise (Bernard et al., 2019). This implies that the style and history of deformation may be more important in controlling natural sample LPO, and perhaps, by inference, seismic anisotropy, particularly in the lithosphere where deformation is commonly more localized and where preservation potential is high.

Besides these uncertainties regarding the formation of different LPO types under dislocation creep by changes in slip system activity due to ambient conditions, it is not straightforward to predict where dislocation creep should dominate (Hirth and Kohlstedt, 2004). The estimate of predominant dislocation creep between ~100–300 km for grain sizes of order mm (Podolefsky et al., 2004) is compatible with the depth distribution of radial anisotropy, for example (Becker et al., 2008; Behn et al., 2009). However, using different assumptions about grain growth and evolution, Dannberg et al. (2017) constructed mantle convection models, which are consistent with seismic attenuation, but would predict the dominance of diffusion creep within the asthenosphere. The assumption that LPOs only form under dislocation creep and are preserved or destroyed under diffusion creep has been challenged (e.g., Sundberg and Cooper, 2008; Miyazaki et al., 2013; Maruyama and Hiraga, 2017), but it remains to be seen where most of the discrepancies arise.

While geodynamic modeling can easily incorporate stress, temperature, and pressure-dependent changes in slip systems for LPO predictions, for example, it is thus not clear if such a modeling approach is warranted. If volatile content is used as a free parameter, for example, we can construct upper mantle models with a range of seismic anisotropy predictions for the exact same convective model. This is not the most satisfying situation, unless other constraints such as from magneto-tellurics or phase boundary deflections provide further constraints on volatile variations. Moreover, the good match of the geodynamic reference model to azimuthal and radial anisotropy discussed in Section 10.3.3 implies that A type LPO, formed under dislocation creep, may well be dominant in the upper mantle.

Mechanical Anisotropy. Besides seismic, we also expect mechanical anisotropy as a result of the formation of LPO, i.e., the deformation behavior of olivine will depend on the sense and type of shear. Such viscous anisotropy is one potential mechanism for lithospheric strain-localization and deformation memory in plate boundaries (e.g., Tommasi et al., 2009; Montési, 2013). Mechanical anisotropy has been documented in the laboratory for olivine LPO (Hansen et al., 2012), and was implemented in microstructural modeling approaches (Castelnau et al., 2009; Hansen et al., 2016c).

We expect viscous anisotropy to increase the wavelength of convection (Honda, 1986; Busse et al., 2006) and localize flow in the asthenosphere if the weak plane is aligned with plate shear, possibly stabilizing time-dependent plate motions (Christensen, 1987; Becker and Kawakatsu, 2011). The response of a mechanically anisotropic layer will also lead to a modification of the growth rates of folding or density driven instabilities (Mühlhaus et al., 2002; Lev and Hager, 2008). However, trade-offs between isotropically weakened layers and anisotropic viscosity may make any effects on post-glacial response, the geoid, or the planform of convection hard to detect (Han and Wahr, 1997; Becker and Kawakatsu, 2011), in analogy to the bulk seismic anisotropy of a layered medium with isotropic velocity variations (Backus, 1962).

On regional scales, the effect of viscous anisotropy may be more easily seen in tectonic or dynamic observables, and any treatment of the development of texture should in principle account for the mechanical effects of LPO formation on flow for self-consistency and to account for possible feedback mechanisms (Knoll et al., 2009). The joint development of mechanical and seismic anisotropy may be of relevance in subduction zones, where seismic anisotropy is widespread, and time-dependent fluctuations in the mantle wedge temperature may result (Lev and Hager, 2011).

Self-consistent modeling of both seismic and viscous anisotropy was implemented by Chastel et al. (1993) for an idealized convective cell, and more recently by Blackman et al. (2017) for a more complete convection model of a spreading center. Models that include the LPO feedback show generally similar flow patterns than simpler models, but there can be up to a factor ∼2 enhancement of predicted surface wave azimuthal anisotropy close to the ridge because of increased strain-rates, and the transverse isotropy symmetry axes are more horizontally aligned (Blackman et al., 2017) than those of earlier one-way LPO predictions (Blackman and Kendall, 2002). It remains to be seen if such effects of viscous anisotropy feedback are relevant for the interpretation of regional or global convection, or if other uncertainties such as the effects of temperature, composition, and volatile anomalies on isotropic olivine rheology swamp the signal.

10.5. WAYS FORWARD

Our general understanding of upper mantle convection thus appears to be reflected in seismic anisotropy, and anisotropy allows broad inferences on asthenospheric viscosity and regional tectonics, for example. Yet, many uncertainties remain and become most acute if the strength of anisotropy is to be exploited quantitatively. What can we do to raise the water levels of this glass-half-full scenario?

For one, more data, and in particular more seafloor, or oceanic realm, observations, as well as dense continental seismometer deployments, certainly help. Higher-density imaging should resolve many of the uncertainties, including the depth distribution of seismic anisotropy in oceanic plates over the next decade. Seismometer arrays such as USArray have transformed our view of mantle structure under continental plates, even though much work is still to be done to integrate the newly imaged complexity into dynamic models of mantle evolution. Availability of high-density passive seismic data means better resolution for surface wave studies. Moreover, many deployments are now also sampling the upper mantle with strongly overlapping Fresnel zones (3-D sensitivity kernels) for *SKS* splitting (Chevrot et al., 2004; Long et al., 2008). Using methods that make use of the array station density (Ryberg et al., 2005; Abt and Fischer, 2008; Monteiller and Chevrot, 2011; Lin et al., 2014; Mondal and Long, 2019) rather than presenting individual splits without concern as to the likely implications of back-azimuthal dependencies and overlapping sensitivity is still the exception, however. It should become the rule, even if the methodological burden is higher.

Yet, even for well-constrained regions, at least some trade-offs between structural model parameters will likely persist, which is when inversion choices as to parameterization and regularization become even more important. Any mixed- or underdetermined inverse problem requires regularization, and often choices are made based on the intuition, or preconceptions, of seismologists as to the degree of isotropic and anisotropic heterogeneity. Different structural representations can result, depending on the treatment of the preferred spectral character of isotropic and anisotropic heterogeneity. One way to approach the problem is to quantify the statistical character of heterogeneity of anisotropy and isotropic velocity anomalies (e.g., due to temperature and compositional variations) from field observations or convection modeling (e.g., Holliger and Levander, 1992; Becker et al., 2007b; Kennett et al., 2013; Alder et al., 2017), and then have those properties guide regularization.

Another, more narrow, but perhaps in our context more productive, way to introduce a priori information is to use assumptions about the symmetry types of anisotropy and

conditions for the formation of certain LPO types for imaging or joint seismological and geodynamic inversion. This spells out a project to integrate as much information about the link between seismic anisotropy and convection from laboratory and field work, to seismology, to geodynamic modeling for a better understanding of the evolution of plate tectonics. Once firm links are established, such an approach should, in principle, allow extending the use of seismic anisotropy much further back in time than the last few 10s of Myr, if we are able to capture the lithospheric memory of "frozen in" structure alongside the asthenospheric convection contribution.

The simplifications of hexagonal symmetry axes being oriented vertically (radial anisotropy) or horizontally (azimuthal anisotropy) is one example of imposing a priori assumptions to simplify imaging. More generally, we can solve for the overall orientation of the symmetry axes of a medium with hexagonal anisotropy, for example. This approach is called *vectorial tomography* (Montagner and Nataf, 1988; Chevrot, 2006) and has been in use for a long time (Montagner and Jobert, 1988), though not widely so. Vectorial tomography exploits the fact that individual minerals such as olivine show certain characteristics which link different elastic parameters, allowing reduction in the parameter space that has to be explored by a seismological inversion (Montagner and Anderson, 1989; Plomerová et al., 1996; Xie et al., 2015). Similar relationships between parameters such as *P*- and *S*-wave anisotropy, for example, can be established for upper-mantle LPO assemblages (Becker et al., 2006a, 2008) or crustal rocks (Brownlee et al., 2017), and the resulting scaling relationships can improve inversion robustness (Panning and Nolet, 2008; Chevrot and Monteiller, 2009; Xie et al., 2015; Mondal and Long, 2019).

Use of such petrological scalings limits the interpretation to, say, determining the orientation and saturation of a certain type of olivine LPO in the mantle, rather than being general and allowing for other causes of anisotropy. However, the images of lateral variations should be more robust than the general inversion which will itself be subject to other assumptions, even if it is just regularization. Moreover, different assumptions as to which types of LPOs might be present can also be tested in a vectorial tomography framework. In this context, surface wave anomalies in 2φ and 4φ patterns (e.g., Montagner and Tanimoto, 1990; Trampert and Woodhouse, 2003; Visser et al., 2008) also appear underutilized. Based on a simple petrological model for peridotite, *Montagner and Nataf* (1986) showed that mantle-depth Rayleigh and Love waves should be mainly sensitive to the 2φ and 4φ signal, respectively. However, there is evidence for additional Rayleigh and Love wave structure in 4φ and 2φ, respectively, for the mantle (e.g., Trampert and Woodhouse, 2003), and such signals are often seen for the crust (cf. Figure 10.3; e.g., Adam and Lebedev, 2012; Xie et al., 2015). For many petrological models, there exist strong relationships between the 2φ and 4φ signature in each wave type, meaning that Rayleigh and Love waves can be inverted jointly for azimuthal anisotropy for certain a priori assumptions, yet this is not often done (e.g., Xie et al., 2015; Russell et al., 2019) as horizontal records are usually noisier than vertical seismograms. Moreover, the sensitivity of each surface wave type depends on the dip angle and olivine LPO type which might be diagnostic. This could be further utilized in vectorial tomography imaging, particularly for joint surface and body wave inversions (Romanowicz and Yuan, 2012).

In order to proceed with such joint inversions, we need to better understand the predictions of laboratory experiments as to LPO formation under different deformation conditions. This requires more experimental work, particularly under low deviatoric stress (Skemer and Hansen, 2016; Bernard et al., 2019). Moreover, a better handle on the degree to which dislocation creep dominates LPO formation needs to be established. Using improved microstructural relationships, we can also revisit the treatment of grain-size evolution to better explore which parts of the mantle should form anisotropy under what conditions. Among other improvements of time-dependent mantle flow models, such a consistent picture of the across-scale deformation of the upper mantle will not only provide better constraints on convection but also clarify the role of grain-size evolution and inherited fabrics for the formation and preservation of plate boundaries (e.g., Tommasi et al., 2009; Montési, 2013; Bercovici et al., 2015).

10.6. CONCLUSIONS

So, which is it, a can of worms or the most useful constraint? We think that the pitfalls of non-uniqueness and uncertainties in the relationship between convection and seismic observations can be overcome. Using a combination of targeted laboratory experiments, further comparison with field analogs and samples, improved seismological imaging, and geodynamic modeling we can achieve a powerful, integrated interpretation of seismic and other data and models, including those from geodesy, the geological record, mineralogy, and geodynamics. In particular, we look forward to seeing more work using vectorial tomography in multidisciplinarily constrained, densely sampled key study areas. The promise of being able to potentially resolve the depth distribution of shear in convection, and hence mantle rheology, and the potential to unlock the deformation memory of both continental and oceanic plates for a new set of constraints on the mechanisms governing their evolution make the headaches worth while.

ACKNOWLEDGMENTS

We thank Whitney Behr, Donna Blackman, and Clint Conrad as well as Barbara Romanowicz and an anonymous reviewer who provided very helpful comments on an earlier version of this manuscript. Most plots were made with the Generic Mapping Tools (Wessel and Smith, 1998). TWB was partly supported by the National Science Foundation (NSF) under grant EAR-1460479. This publication has emanated from research supported in part by research grants from Science Foundation Ireland (SFI) under grant numbers 16/IA/4598 and 13/RC/2092, co-funded under the European Regional Development Fund and by iCRAG industry partners.

REFERENCES

Abt, D. L., & K. M. Fischer (2008). Resolving three-dimensional anisotropic structure with shear-wave splitting tomography, *Geophys. J. Int.*, *173*, 859–886.

Adam, J. M.-C., & S. Lebedev (2012). Azimuthal anisotropy beneath southern Africa from very broad-band surface-wave dispersion measurements, *Geophys. J. Int.*, *191*, 155–174.

Agius, M. R., & S. Lebedev (2014). Shear-velocity structure, radial anisotropy and dynamics of the Tibetan crust, *Geophys. J. Int.*, *199*, 1395–1415.

Agius, M. R., & S. Lebedev (2017). Complex, multilayered azimuthal anisotropy beneath Tibet: evidence for co-existing channel flow and pure-shear crustal thickening, *Geophys. J. Int.*, *210*, 1823–1844.

Aki, K., & K. Kaminuma (1963). Phase velocity in Japan. Part I. Love waves from the Aleutian shock of March 9, 1957, *Bull. Earthq. Res. Inst. Tokyo Univ*., *41*, 243–259.

Alder, C., T. Bodin, Y. Ricard, Y. Capdeville, E. Debayle, & J. P. Montagner (2017). Quantifying seismic anisotropy induced by small-scale chemical heterogeneities, *Geophys. J. Int.*, *211*, 1585–1600.

Alisic, L., M. Gurnis, G. Stadler, C. Burstedde, & O. Ghattas (2012). Multi-scale dynamics and rheology of mantle flow with plates, *J. Geophys. Res.*, *117*(B10402), doi:10.1029/2012JB009234.

Alpert, L. A., M. S. Miller, T. W. Becker, & A. A. Allam (2013). Structure beneath the Alboran from geodynamic flow models and seismic anisotropy, *J. Geophys. Res.*, *118*, 1–13, doi:10.1002/jgrb.50309.

Anderson, D. L. (1961). Elastic wave propagation in layered anisotropic media, *J. Geophys. Res.*, *66*, 2953–2963.

Anderson, D. L. (1989). *Theory of the Earth*, Blackwell Scientific Publications, Boston, available online at http://resolver.caltech.edu/CaltechBOOK:1989.001, accessed 01/2019.

Anderson, D. L., & A. M. Dziewoński (1982). Upper mantle anisotropy: evidence from free oscillations, *Geophys. J. R. Astr. Soc.*, *69*, 383–404.

Auer, L., L. Boschi, T. W. Becker, T. Nissen-Meyer, & D. Giardini (2014). Savani: A variable-resolution whole-mantle model of anisotropic shear-velocity variations based on multiple datasets, *J. Geophys. Res.*, *119*, 3006–3034, doi: 10.1002/2013JB010773.

Auer, L., T. W. Becker, L. Boschi, & N. Schmerr (2015). Thermal structure, radial anisotropy, and dynamics of oceanic boundary layers, *Geophys. Res. Lett.*, *42*, 9740–9742, doi:10.1002/2015GL066246.

Babuška, V., J.-P. Montagner, J. Plomerová, & N. Girardin (1998). Age-dependent large-scale fabric of the mantle lithosphere as derived from surface-wave velocity anisotropy, *Pure Appl. Geophys.*, *151*, 257–280.

Backus, G. E. (1962). Long-wave elastic anisotropy produced by horizontal layering, *J. Geophys. Res.*, *67*, 4427–4440.

Backus, G. E. (1965). Possible forms of seismic anisotropy of the uppermost mantle under oceans, *J. Geophys. Res.*, *70*, 3429–3439.

Bamford, D. (1977). Pn velocity anisotropy in a continental upper mantle, *Geophys. J. R. Astr. Soc.*, *49*, 29–48.

Becker, T. W. (2006). On the effect of temperature and strain-rate dependent viscosity on global mantle flow, net rotation, and plate-driving forces, *Geophys. J. Int.*, *167*, 943–957.

Becker, T. W. (2008). Azimuthal seismic anisotropy constrains net rotation of the lithosphere, *Geophys. Res. Lett*., *35* (L05303). doi:10.1029/2007GL032928, correction: doi:10.1029/2008GL033946.

Becker, T. W. (2017). Superweak asthenosphere in light of upper-mantle seismic anisotropy, *Geochem., Geophys*., *Geosys.*, *18*, 1986–2003, doi:10.1002/2017GC006886.

Becker, T. W., & H. Kawakatsu (2011). On the role of anisotropic viscosity for plate-scale flow, *Geophys. Res. Lett.*, *38* (L17307). doi:10.1029/2011GL048584.

Becker, T. W., & R. J. O'Connell (2001). Predicting plate velocities with geodynamic models, *Geochem., Geophys., Geosys*., *2*(12). doi:10.1029/2001GC000171.

Becker, T. W., J. B. Kellogg, G. Ekström, & R. J. O'Connell (2003). Comparison of azimuthal seismic anisotropy from surface waves and finite-strain from global mantle-circulation models, *Geophys. J. Int.*, *155*, 696–714.

Becker, T. W., S. Chevrot, V. Schulte-Pelkum, & D. K. Blackman (2006a). Statistical properties of seismic anisotropy predicted by upper mantle geodynamic models, *J. Geophys. Res*., *111*(B08309). doi:10.1029/2005JB004095.

Becker, T. W., V. Schulte-Pelkum, D. K. Blackman, J. B. Kellogg, & R. J. O'Connell (2006b). Mantle flow under the western United States from shear wave splitting, *Earth Planet. Sci. Lett.*, *247*, 235–251.

Becker, T. W., G. Ekström, L. Boschi, & J. W. Woodhouse (2007a). Length-scales, patterns, and origin of azimuthal seismic anisotropy in the upper mantle as mapped by Rayleigh waves, *Geophys. J. Int.*, *171*, 451–462.

Becker, T. W., J. T. Browaeys, & T. H. Jordan (2007b). Stochastic analysis of shear wave splitting length scales, *Earth Planet. Sci. Lett.*, *259*, 29–36.

Becker, T. W., B. Kustowski, & G. Ekström (2008). Radial seismic anisotropy as a constraint for upper mantle rheology, *Earth Planet. Sci. Lett.*, *267*, 213–237.

Becker, T. W., S. Lebedev, & M. D. Long (2012). On the relationship between azimuthal anisotropy from shear wave splitting and surface wave tomography, *J. Geophys. Res*., *117* (B01306). doi:10.1029/2011JB008705, original and updated splitting data base available online from http://www-udc.ig.utexas.edu/external/becker/sksdata.html, accessed 01/2019.

Becker, T. W., C. P. Conrad, A. J. Schaeffer, & S. Lebedev (2014). Origin of azimuthal seismic anisotropy in oceanic plates and mantle, *Earth Planet. Sci. Lett.*, *401*, 236–250.

Becker, T. W., A. J. Schaeffer, S. Lebedev, & S. P. Conrad (2015). Toward a generalized plate motion reference frame, *Geophys. Res. Lett.*, *42*, 3188–3196, doi: 10.1002/2015GL063695.

Beghein, C., & J. Trampert (2004). Probability density functions for radial anisotropy: implications for the upper 1200 km of the mantle, *Earth Planet. Sci. Lett.*, *217*, 151–162.

Beghein, C., J. Trampert, & H. J. van Heijst (2006). Radial anisotropy in seismic reference models of the mantle, *J. Geophys. Res.*, *111*, doi:10.1029/2005JB00372.

Beghein, C., J. Resovsky, & R. D. van der Hilst (2008). The signal of mantle anisotropy in the coupling of normal modes, *Geophys. J. Int.*, *175*, 1209–1234.

Beghein, C., K. Yuan, N. Schmerr, & Z. Xing (2014). Changes in seismic anisotropy shed light on the nature of the Gutenberg discontinuity, *Science*, *343*, 1237–1240.

Behn, M. D., C. P. Conrad, & P. G. Silver (2004). Detection of upper mantle flow associated with the African Superplume, *Earth Planet. Sci. Lett.*, *224*, 259–274.

Behn, M. D., G. Hirth, & J. R. Elsenbeck II (2009). Implications of grain size evolution on the seismic structure of the oceanic upper mantle, *Earth Planet. Sci. Lett.*, *282*, 178–189.

Ben Ismail, W., & D. Mainprice (1998). An olivine fabric database; an overview of upper mantle fabrics and seismic anisotropy, *Tectonophys.*, *296*, 145–157.

Bensen, G. D., M. H. Ritzwoller, M. P. Barmin, A. L. Levshin, F. Lin, M. P. Moschetti, N. M. Shapiro, & Y. Yang (2007). Processing seismic ambient noise data to obtain reliable broad-band surface wave dispersion measurements, *Geophys. J. Int.*, *169*, 1239–1260.

Bercovici, D., P. T. Tackley, & Y. Ricard (2015). The generation of plate tectonics from mantle convection, in *Treatise on Geophysics,* 2 ed., pp. 271–318, Elsevier.

Bernard, R., W. M. Behr, T. W. Becker, & D. Young (2019). Relationships between olivine CPO and deformation parameters in naturally deformed rocks and implications for mantle seismic anisotropy, *Geochem., Geophys., Geosys.*, doi: 10.1002/2019GC008289.

Blackman, D., D. Boyce, O. Castelnau, P. R. Dawson, & G. Laske (2017). Effects of crystal preferred orientation on upper-mantle flow near plate boundaries: rheologic feedbacks and seismic anisotropy, *Geophys. J. Int.*, *210*, 1481–1493.

Blackman, D. K., & J.-M. Kendall (1997). Sensitivity of teleseismic body waves to mineral texture and melt in the mantle beneath a mid-ocean ridge, *Phil. Trans. Roy. Soc. Lond. A*, *235*, 217–231.

Blackman, D. K., & J.-M. Kendall (2002). Seismic anisotropy of the upper mantle: 2. Predictions for current plate boundary flow models, *Geochem., Geophys., Geosys.*, *3*(2001GC000247).

Blackman, D. K., J.-M. Kendall, P. R. Dawson, & H.-R. Wenk (1996). Teleseismic imaging of subaxial flow at mid-ocean ridges: traveltime effects of anisotropic mineral texture in the mantle, *Geophys. J. Int.*, *127*, 415–426.

Blackman, D. K., H.-R. Wenk, & J.-M. Kendall (2002). Seismic anisotropy of the upper mantle: 1. Factors that affect mineral texture and effective elastic properties, *Geochem., Geophys., Geosys.*, *3*(2001GC000248).

Bodin, T., J. Leiva, B. A. Romanowicz, V. Maupin, & H. Yuan (2016). Imaging anisotropic layering with Bayesian inversion of multiple data types, *Geophys. J. Int.*, *206*, 605–629.

Boneh, Y., L. F. Morales, É. Kaminski, & P. Skemer (2015). Modeling olivine CPO evolution with complex deformation histories: Implications for the interpretation of seismic anisotropy in the mantle, *Geochem., Geophys., Geosys.*, *16*(10). 3436–3455, doi:10.1002/2015GC005964.

Boneh, Y., D. Wallis, L. N. Hansen, M. Krawczynski, & P. Skemer (2017). Oriented grain growth and modification of "frozen anisotropy" in the lithospheric mantle, *Earth Planet. Sci. Lett.*, *474*, 368–374.

Browaeys, J., & S. Chevrot (2004). Decomposition of the elastic tensor and geophysical applications, *Geophys. J. Int.*, *159*, 667–678.

Brownlee, S. J., V. Schulte-Pelkum, A. Raju, K. Mahan, C. Condit, & O. F. Orlandini (2017). Characteristics of deep crustal seismic anisotropy from a compilation of rock elasticity tensors and their expression in receiver functions, *Tectonics*, *36*, 1835–1857, doi:10.1002/2017TC004625.

Buehler, J. S., & P. M. Shearer (2010). *Pn* tomography of the western United States using US Array, *J. Geophys. Res.*, *115*(B09315). doi:10.1029/2009JB006874.

Burgos, G., J.-P. Montagner, E. Beucler, Y. Capdeville, A. Mocquet, & M. Drilleau (2014). Oceanic lithosphere/asthenosphere boundary from surface wave dispersion data, *J. Geophys. Res.*, *119*, 1079–1093, doi:10.1002/2013JB010528.

Busse, F. H., M. A. Richards, & A. Lenardic (2006). A simple model of high Prandtl and high Rayleigh number convection bounded by thin low-viscosity layers, *Geophys. J. Int.*, *164*, 160–167.

Buttles, J., & P. Olson (1998). A laboratory model of subduction zone anisotropy, *Earth Planet. Sci. Lett.*, *164*, 245–262.

Bystricky, M., K. Kunze, L. Burlini, & J.-P. Burg (2000). High shear strain of olivine aggregrates: rheological and seismic consequences, *Science*, *290*, 1564–1567.

Castelnau, O., D. K. Blackman, & T. W. Becker (2009). Numerical simulations of texture development and associated rheological anisotropy in regions of complex mantle flow, *Geophys. Res. Lett.*, *36*(L12304). doi:10.1029/2009GL038027.

Chang, S.-J., A. M. G. Ferreira, J. Ritsema, H. J. van Heijst, & J. H. Woodhouse (2015). Joint inversion for global isotropic and radially anisotropic mantle structure including crustal thickness perturbations, *J. Geophys. Res.*, *120*, 4278–4300, doi:10.1002/2014JB011824.

Chase, C. G. (1978). Extension behind island arcs and motion relative to hot spots, *J. Geophys. Res.*, *83*, 5385–5387.

Chastel, Y. B., P. R. Dawson, H.-R. Wenk, & K. Bennett (1993). Anisotropic convection with implications for the upper mantle, *J. Geophys. Res.*, *98*, 17,757–17,771.

Chevrot, S. (2006). Finite-frequency vectorial tomography: a new method for high-resolution imaging of upper mantle anisotropy, *Geophys. J. Int.*, *165*, 641–657.

Chevrot, S., & V. Monteiller (2009). Principles of vectorial tomography – the effects of model parametrization and regularization in tomographic imaging of seismic anisotropy, *Geophys. J. Int.*, *179*, 1726–1736.

Chevrot, S., N. Favier, & D. Komatitsch (2004). Shear wave splitting in three-dimensional anisotropic media, *Geophys. J. Int.*, *159*, 711–720.

Christensen, U. R. (1987). Some geodynamical effects of anisotropic viscosity, *Geophys. J. R. Astr. Soc.*, *91*, 711–736.

Conrad, C. P., & M. D. Behn (2010). Constraints on lithosphere net rotation and asthenospheric viscosity from global mantle flow models and seismic anisotropy, *Geochem., Geophys., Geosys.*, *11*(Q05W05). doi:10.1029/2009GC002970.

Conrad, C. P., & M. Gurnis (2003). Seismic tomography, surface uplift, and the breakup of Gondwanaland: Integrating mantle convection backwards in time, *Geochem., Geophys., Geosys., 4*(2001GC000299).

Conrad, C. P., & C. Lithgow-Bertelloni (2002). How mantle slabs drive plate tectonics, *Science*, *298*, 207–209.

Conrad, C. P., & C. Lithgow-Bertelloni (2007). Faster seafloor spreading and lithosphere production during the mid-Cenozoic, *Geology*, *35*, 29–32.

Conrad, C. P., M. D. Behn, & P. G. Silver (2007). Global mantle flow and the development of seismic anisotropy: Differences between the oceanic and continental upper mantle, *J. Geophys. Res.*, *112*(B07317). doi:10.1029/2006JB004608.

Crampin, S., & S. Chastin (2003). A review of shear wave splitting in the crack-critical crust, *Geophys. J. Int.*, *155*, 221–240.

Dahlen, F. A., & J. Tromp (1998). *Theoretical Global Seismology*, Princeton University Press, Princeton, New Jersey.

Dannberg, J., Z. Eilon, U. Faul, R. Gassmöller, P. Moulik, & R. Myhill (2017). The importance of grain size to mantle dynamics and seismological observations, *Geochem., Geophys., Geosys.*, *18*, 3034–3061, doi:10.1002/2017GC006944.

Debayle, E., & Y. Ricard (2013). Seismic observations of large-scale deformation at the bottom of fast-moving plates, *Earth Planet. Sci. Lett.*, *376*, 165–177.

DeMets, C., R. G. Gordon, & D. F. Argus (2010). Geologically current plate motions, *Geophys. J. Int.*, *181*, 1–80.

Deschamps, F., S. Lebedev, T. Meier, & J. Trampert (2008a). Azimuthal anisotropy of Rayleigh-wave phase velocities in the east-central United States, *Geophys. J. Int.*, *173*, 827–843.

Deschamps, F., S. Lebedev, T. Meier, & J. Trampert (2008b). Stratified seismic anisotropy reveals past and present deformation beneath the East-central United States, *Earth Planet. Sci. Lett.*, *274*, 489–498.

Dziewoński, A. M., & D. L. Anderson (1981). Preliminary reference Earth model, *Phys. Earth Planet. Inter.*, *25*, 297–356.

Ekström, G. (2011). A global model of Love and Rayleigh surface wave dispersion and anisotropy, 25–250 s, *Geophys. J. Int.*, *187*, 1668–1686.

Ekström, G., & A. M. Dziewoński (1998). The unique anisotropy of the Pacific upper mantle, *Nature*, *394*, 168–172.

Ekström, G., J. Tromp, & E. Larson (1997). Measurements and global models of surface wave propagation, *J. Geophys. Res.*, *102*, 8137–8157.

Ekström, G., G. A. Abers, & S. C. Webb (2009). Determination of surface-wave phase velocities across USArray from noise and Aki's spectral formulation, *Geophys. Res. Lett.*, *36* (L18301). doi:10.1029/2009GL039131.

Faccenda, M., & F. A. Capitanio (2013). Seismic anisotropy around subduction zones: Insights from three-dimensional modeling of upper mantle deformation and SKS splitting calculations, *Geochem., Geophys., Geosys.*, *14*, doi: 10.1029/2012GC004451.

Faccenna, C., T. W. Becker, L. Jolivet, & M. Keskin (2013). Mantle convection in the Middle East: Reconciling Afar upwelling, Arabia indentation and Aegean trench rollback, *Earth Planet. Sci. Lett.*, *375*, 254–269.

Farra, V., & L. Vinnik (2002). Upper mantle stratification by P and S receiver functions, *Geophys. J. Int.*, *141*, 699–712.

Ferreira, A. M. G., J. H. Woodhouse, K. Visser, & J. Trampert (2010). On the robustness of global radially anisotropic surface wave tomography, *J. Geophys. Res.*, *115*(B04313). doi:10.1029/2009JB006716.

Fichtner, A., B. L. N. Kennett, & J. Trampert (2013). Separating intrinsic and apparent anisotropy, *Phys. Earth Planet. Inter.*, *219*, 11–20.

Fischer, K. M., & D. A. Wiens (1996). The depth distribution of mantle anisotropy beneath the Tonga subduction zone, *Earth Planet. Sci. Lett.*, *142*, 253–260.

Forsyth, D. W. (1975). The early structural evolution and anisotropy of the oceanic upper mantle, *Geophys. J. R. Astr. Soc.*, *43*, 103–162.

Forte, A. M., W. R. Peltier, & A. M. Dziewoński (1991). Inferences of mantle viscosity from tectonic plate velocities, *Geophys. Res. Lett.*, *18*, 1747–1750.

Fouch, M. J., & K. M. Fischer (1996). Mantle anisotropy beneath Northwest Pacific subduction zones, *J. Geophys. Res.*, *101*, 15,987–16,002.

Fouch, M. J., K. M. Fischer, E. M. Parmentier, M. E. Wysession, & T. J. Clarke (2000). Shear wave splitting, continental keels, and patterns of mantle flow, *J. Geophys. Res.*, *105*, 6255–6275.

French, S. W., & B. A. Romanowicz (2014). Whole-mantle radially anisotropic shear velocity structure from spectral-element waveform tomography, *Geophys. J. Int.*, *199*, 1303–1327.

Funiciello, F., C. Faccenna, A. Heuret, E. Di Giuseppe, S. Lallemand, & T. W. Becker (2008). Trench migration, net rotation and slab-mantle coupling, *Earth Planet. Sci. Lett.*, *271*, 233–240.

Gaboret, C., A. M. Forte, & J.-P. Montagner (2003). The unique dynamics of the Pacific Hemisphere mantle and its signature on seismic anisotropy, *Earth Planet. Sci. Lett.*, *208*, 219–233.

Gaherty, J. B., & T. H. Jordan (1995). Lehmann discontinuity as the base of an anisotropic layer beneath continents, *Science*, *268*, 1468–1471.

Gaherty, J. B., T. H. Jordan, & L. S. Gee (1996). Seismic structure of the upper mantle in a central Pacific corridor, *J. Geophys. Res.*, *101*, 22,291–22,310.

Gaherty, J. B., D. Lizarralde, J. A. Collins, G. Hirth, & S. Kim (2004). Mantle deformation during slow seafloor spreading constrained by observations of seismic anisotropy in the western Atlantic, *Earth Planet. Sci. Lett.*, *228*, 225–265.

Godfrey, N. J., N. I. Christensen, & D. A. Okaya (2000). Anisotropy of schists: Contribution of crustal anisotropy to active source seismic experiments and shear wave splitting observations, *J. Geophys. Res.*, *105*, 27,991–28,007.

Goulding, N. J., N. M. Ribe, O. Castelnau, A. M. Walker, & J. Wookey (2015). Analytical parametrization of self-consistent polycrystal mechanics: Fast calculation of upper mantle anisotropy, *Geophys. J. Int.*, *203*, 334–350.

Gung, Y., M. Panning, & B. A. Romanowicz (2003). Global anisotropy and the thickness of continents, *Nature*, *422*, 707–711.

Hager, B. H. (1984). Subducted slabs and the geoid: constraints on mantle rheology and flow, *J. Geophys. Res.*, *89*, 6003–6015.

Hager, B. H., & R. J. O'Connell (1981). A simple global model of plate dynamics and mantle convection, *J. Geophys. Res.*, *86*, 4843–4867.

Hager, B. H., R. W. Clayton, M. A. Richards, R. P. Comer, & A. M. Dziewoński (1985). Lower mantle heterogeneity, dynamic topography and the geoid, *Nature*, *313*, 541–545.

Hall, C. E., K. M. Fischer, E. M. Parmentier, & D. K. Blackman (2000). The influence of plate motions on three-dimensional back arc mantle flow and shear wave splitting, *J. Geophys. Res.*, *105*, 28,009–28,033.

Han, D., & J. Wahr (1997). An analysis of anisotropic mantle viscosity, and its possible effects on post-glacial rebound, *Phys. Earth Planet. Inter.*, *102*, 33–50.

Hansen, L. N., M. E. Zimmerman, & D. L. Kohlstedt (2012). Laboratory measurements of the viscous anisotropy of olivine aggregates, *Nature*, *492*, 415–418.

Hansen, L. N., Y.-H. Zhao, M. E. Zimmerman, & D. L. Kohlstedt (2014). Protracted fabric evolution in olivine: Implications for the relationship among strain, crystallographic fabric, and seismic anisotropy, *Earth Planet. Sci. Lett.*, *387*, 157–158.

Hansen, L. N., C. Qib, & J. M. Warren (2016a). Olivine anisotropy suggests Gutenberg discontinuity is not the base of the lithosphere, *Proc. Natl. Acad. Sci. USA*, *113*, 10,503–10,506.

Hansen, L. N., C. P. Conrad, Y. Boneh, P. Skemer, J. M. Warren, & D. L. Kohlstedt (2016b). Viscous anisotropy of textured olivine aggregates: 2. Micromechanical model, *J. Geophys. Res.*, *121*, 7137–7160, doi:10.1002/2016JB013240.

Hansen, L. N., J. M. Warren, M. E. Zimmerman, & D. L. Kohlstedt (2016c). Viscous anisotropy of textured olivine aggregates, Part 1: Measurement of the magnitude and evolution of anisotropy, *Earth Planet. Sci. Lett.*, *445*, 92–103.

Hess, H. H. (1964). Seismic anisotropy of the uppermost mantle under oceans, *Nature*, *203*, 629–631.

Hirth, G., & D. L. Kohlstedt (2004). Rheology of the upper mantle and the mantle wedge: A view from the experimentalists, in *Inside the Subduction Factory, Geophys. Monograph*, vol. *138*, edited by J. Eiler, pp. 83–105, American Geophysical Union, Washington DC.

Holliger, K., & A. R. Levander (1992). A stochastic view of lower crustal fabric based on evidence from the Ivrea Zone, *Geophys. Res. Lett.*, *19*, 1153–1156.

Holtzman, B. K., & J. Kendall (2010). Organized melt, seismic anisotropy, and plate boundary lubrication, *Geochem., Geophys., Geosys.*, *11*(Q0AB06). doi:10.1029/ 2010GC003296.

Holtzman, B. K., D. L. Kohlstedt, M. E. Zimmerman, F. Heidelbach, T. Hiraga, & J. Hustoft (2003). Melt segregation and strain partitioning: Implications for seismic anisotropy and mantle flow, *Science*, *301*, 1227–1230.

Honda, S. (1986). Strong anisotropic flow in a finely layered asthenosphere, *Geophys. Res. Lett.*, *13*, 1454–1457.

Hu, J., M. Faccenda, & L. Liu (2017). Subduction-controlled mantle flow and seismic anisotropy in South America, *Earth Planet. Sci. Lett.*, *470*, 13–24.

Husson, L., P. Yamato, & A. Bézos (2015). Ultraslow, slow, or fast spreading ridges: Arm wrestling between mantle convection and far-field tectonics, *Earth Planet. Sci. Lett.*, *429*, 205–215.

Ishise, M., & H. Oda (2005). Three-dimensional structure of P-wave anisotropy beneath the Tohoku district, northeast Japan, *J. Geophys. Res.*, *110*(B07304). doi: 10.1029/ 2004JB003599.

Isse, T., H. Kawakatsu, K. Yoshizawa, A. Takeo, H. Shiobara, H. Sugioka, A. Ito, D. Suetsugu, & D. Reymond (2019). Surface wave tomography for the Pacific Ocean incorporating seafloor seismic observations and plate thermal evolution, *Earth Planet. Sci. Lett.*, *510*, 116–130.

Ito, G., R. Dunn, A. Li, C. J. Wolfe, A. Gallego, & Y. Fu (2014). Seismic anisotropy andshear wave splitting associated with mantle plume-plate interaction, *J. Geophys. Res.*, *119*, 4923–4937, doi:10.1002/2013JB010735.

Jung, H., & S.-i. Karato (2001). Water-induced fabric transitions in olivine, *Science*, *293*, 1460–1463.

Jung, H., W. Mo, & H. W. Green (2009). Upper mantle seismic anisotropy resulting from pressure-induced slip transitions in olivine, *Nature Geosc.*, *2*, 73–77.

Kaminski, É. (2002). The influence of water on the development of lattice preferred orientation in olivine aggregates, *Geophys. Res. Lett.*, *29*, 10.1029/2002GL014,710.

Kaminski, É., & N. M. Ribe (2001). A kinematic model for for recrystallization and texture development in olivine polycrystals, *Earth Planet. Sci. Lett.*, *189*, 253–267.

Kaminski, É., & N. M. Ribe (2002). Time scales for the evolution of seismic anisotropy in mantle flow, *Geochem., Geophys., Geosys.*, *3*(2001GC000222).

Kaminski, É., N. M. Ribe, & J. T. Browaeys (2004). D-Rex, a program for calculation of seismic anisotropy due to crystal lattice preferred orientation in the convective upper mantle, *Geophys. J. Int.*, *157*, 1–9.

Karato, S.-i. (1992). On the Lehmann discontinuity, *Geophys. Res. Lett.*, *51*, 2255–2258.

Karato, S.-i. (1998). Seismic anisotropy in the deep mantle, boundary layers and the geometry of convection, *Pure Appl. Geophys.*, *151*, 565–587.

Karato, S.-i., H. Jung, I. Katayama, & P. Skemer (2008). Geodynamic significance of seismic anisotropy of the upper mantle: new insights from laboratory studies, *Ann Rev. Earth Planet. Sci.*, *36*, 59–95.

Katayama, I., H. Jung, & S.-i. Karato (2004). New type of olivine fabric from deformation experiments at modest water content and low stress, *Geology*, *32*, 1045–1048.

Kawakatsu, H. (2016). A new fifth parameter for transverse isotropy, *Geophys. J. Int.*, *204*, 682–685.

Kawakatsu, H., & H. Utada (2017). Seismic and electrical signatures of the litho-sphere-asthenosphere system of the normal oceanic mantle, *Ann. Rev. Earth Planet. Sci.*, *45*, 139–167.

Kawakatsu, H., P. Kumar, Y. Takei, M. Shinohara, T. Kanazawa, E. Araki, & K. Suyehiro (2009). Seismic evidence for sharp lithosphere-asthenosphere boundaries of oceanic plates, *Science*, *324*, 499–502.

Kennett, B. L., & T. Furumura (2013). High-frequency Po/So guided waves in the oceanic lithosphere: long-distance propagation, *Geophys. J. Int.*, *195*, 1862–1877.

King, S. D., & G. Masters (1992). An inversion for radial viscosity structure using seismic tomography, *Geophys. Res. Lett.*, *19*, 1551–1554.

Kneller, E. A., P. E. van Keken, S.-i. Karato, & J. Park (2005). B-type olivine fabric in the mantle wedge: insights from high-resolution non-newtonian subduction zone models, *Earth Planet. Sci. Lett.*, *237*, 781–797.

Knoll, M., A. Tommasi, R. Logé, & J. Signorelli (2009). A multiscale approach to model the anisotropic deformation of lithospheric plates, *Geochem., Geophys., Geosys.*, *10*(Q08009). doi:10.1029/2009GC002423.

Kosarev, G. L., L. I. Makeyeva, & L. P. Vinnik (1984). Anisotropy of the mantle inferred from observations of P to S converted waves, *Geophys. J. R. Astr. Soc.*, *76*, 209–220.

Kreemer, C. (2009). Absolute plate motions constrained by shear wave splitting orientations with implications for hot spot motions and mantle flow, *J. Geophys. Res.*, *114* (B10405). doi:10.1029/2009JB006416.

Kustowski, B., G. Ekström, & A. M. Dziewoński (2008). Anisotropic shear-wave velocity structure of the Earth's mantle: A global model, *J. Geophys. Res.*, *113*, doi:10.1029/2007JB005169.

Laske, G., & G. Masters (1998). Surface-wave polarization data and global anisotropic structure, *Geophys. J. Int.*, *132*, 508–520.

Lassak, T. M., M. J. Fouch, C. E. Hall, & É. Kaminski (2006). Seismic characterization of mantle flow in subduction systems: Can we resolve a hydrated mantle wedge?, *Earth Planet. Sci. Lett.*, *243*, 632–649.

Lebedev, S., G. Nolet, T. Meier, & R. D. van der Hilst (2005). Automated multimode inversion of surface and S waveforms, *Geophys. J. Int.*, *162*, 951–964.

Lebedev, S., T. Meier, & R. D. van der Hilst (2006). Asthenospheric flow and origin of volcanism in the Baikal Rift area, *Earth Planet. Sci. Lett.*, *249*, 415–424.

Lev, E., & B. H. Hager (2008). Rayleigh-Taylor instabilities with anisotropic lithospheric viscosity, *Geophys. J. Int.*, *173*, 806–814.

Lev, E., & B. H. Hager (2011). Anisotropic viscosity changes subduction zone thermal structure, *Geochem., Geophys., Geosys.*, *12*(Q04009). doi:10.1029/ 2010GC003382.

Lin, F. C., M. H. Ritzwoller, Y. Yang, M. P. Moschetti, & M. J. Fouch (2011). Complex and variable crustal and uppermost mantle seismic anisotropy in the western United States, *Nature Geosci.*, *4*, 55–61.

Lin, P.-Y. P., J. B. Gaherty, J. G., J. A. Collins, D. Lizarralde, R. L. Evans, & G. Hirth (2016). High-resolution seismic constraints on flow dynamics in the oceanic asthenosphere, *Nature*, *535*, 538–541.

Lin, Y.-P., L. Zhao, & S.-H. Hung (2014). Full-wave multiscale anisotropy tomography in Southern California, *Geophys. Res. Lett.*, *41*, 8809–8817, doi:10.1002/2014GL061855.

Lithgow-Bertelloni, C., & M. A. Richards (1998). The dynamics of Cenozoic and Mesozoic plate motions, *Rev. Geophys.*, *36*, 27–78.

Long, M. D. (2013). Constraints on subduction geodynamics from seismic anisotropy, *Rev. Geophys.*, *51*, 76–112.

Long, M. D., & T. W. Becker (2010). Mantle dynamics and seismic anisotropy, *Earth Planet. Sci. Lett.*, *297*, 341–354.

Long, M. D., & R. D. van der Hilst (2006). Shear wave splitting from local events beneath the Ryukyu arc: Trench-parallel anisotropy in the mantle wedge, *Phys. Earth Planet. Inter.*, *155*, 300–312.

Long, M. D., M. V. de Hoop, & R. D. van der Hilst (2008). Wave equation shear wave splitting tomography, *Geophys. J. Int.*, *172*, 311–330.

Ma, Z. T., & G. Masters (2015). Effect of earthquake locations on Rayleigh wave azimuthal anisotropy models, *Geophys. J. Int.*, *203*, 1319–1333.

Mainprice, D. (2007). Seismic anisotropy of the deep Earth from a mineral and rock physics perspective, in *Treatise on Geophysics*, vol. *2*, edited by G. Schubert and D. Bercovici, pp. 437–492, Elsevier.

Mainprice, D., A. Tommasi, H. Couvy, P. Cordier, & N. J. J. Frost (2005). Pressure sensitivity of olivine slip systems and seismic anisotropy of Earth's upper mantle, *Nature*, *433*, 731–733.

Marone, F., & B. A. Romanowicz (2007). The depth distribution of azimuthal anisotropy in the continental upper mantle, *Nature*, *447*, 198–201.

Maruyama, G., & T. Hiraga (2017). Grain- to multiple-grain-scale deformation processes during diffusion creep of forsterite + diopside aggregate: 2. Grain boundary sliding-induced grain rotation and its role in crystallographic preferred orientation in rocks, *J. Geophys. Res.*, *122*, 5916–5934, doi:10.1002/2017JB014255.

McEvilly, T. V. (1964). Central U.S. crustâĂŤUpper mantle structure from Love and Rayleigh wave phase velocity inversion, *Bull. Seismol. Soc. Am.*, *54*, 1997–2015.

McKenzie, D. P. (1979). Finite deformation during fluid flow, *Geophys. J. R. Astr. Soc.*, *58*, 689–715.

McNamara, A., S.-i. Karato, & P. E. van Keken (2001). Localization of dislocation creep in the lower mantle: implications for the origin of seismic anisotropy, *Earth Planet. Sci. Lett.*, *191*, 85–99.

Meier, T., K. Dietrich, B. Stöckhert, & H.-P. Harjes (2004). One-dimensional models of shear wave velocity for the eastern Mediterranean obtained from the inversion of Rayleigh wave phase velocities and tectonic implications, *Geophys. J. Int.*, *156*, 45–58.

Miller, M. S., & T. W. Becker (2012). Mantle flow deflected by interactions between subducted slabs and cratonic keels, *Nat. Geosc.*, *5*, 726–730.

Minster, J. B., & T. H. Jordan (1978). Present-day plate motions, *J. Geophys. Res.*, *83*, 5331–5354.

Miyazaki, T., K. Sueyoshi, & T. Hiraga (2013). Olivine crystals align during diffusion creep of Earth's upper mantle, *Nature*, *502*, 321–327.

Mondal, P., & M. D. Long (2019). A model space search approach to finite-frequency SKS splitting intensity tomography in a reduced parameter space, *Geophys. J. Int.*, *217*, 238–256.

Montagner, J.-P. (1994). What can seismology tell us about mantle convection?, *Rev. Geophys.*, *32*, 115–137.

Montagner, J.-P. (2002). Upper mantle low anisotropy channels below the Pacific plate, *Earth Planet. Sci. Lett.*, *202*, 263–274.

Montagner, J.-P., & D. L. Anderson (1989). Petrological constraints on seismic anisotropy, *Phys. Earth Planet. Inter.*, *54*, 82–105.

Montagner, J.-P., & D. L. Anderson (2015). The Pacific Megagash: A future plate boundary?, in *D. L. Anderson Honor Volume, GSA Spec. Papers,* vol. 514, edited by G. R. Foulger, *Geol. Soc. Amer.*, doi:10.1130/2015.2514(10)âĂŃ.

Montagner, J.-P., & L. Guillot (2000). Seismic anisotropy in the Earth's mantle, in *Problems in Geophysics for the New Millenium*, edited by E. Boschi, G. Ekström, & A. Morelli, pp. 217–253, Istituto Nazionale di Geofisica e Vulcanologia, Editrice Compositori, Bologna, Italy.

Montagner, J.-P., & N. Jobert (1988). Vectorial tomography; II. application to the Indian Ocean, *Geophys. J. Int.*, *94*, 309–344.

Montagner, J.-P., & H.-C. Nataf (1986). A simple method for inverting the azimuthal anisotropy of surface waves, *J. Geophys. Res.*, *91*, 511–520.

Montagner, J.-P., & H. C. Nataf (1988). Vectorial tomography-I. Theory, *Geophys. J.*, *94*, 295–307.

Montagner, J.-P., & T. Tanimoto (1990). Global anisotropy in the upper mantle inferred from the regionalization of phase velocities, *J. Geophys. Res.*, *95*, 4797–4819.

Montagner, J.-P., & T. Tanimoto (1991). Global upper mantle tomography of seismic velocities and anisotropies, *J. Geophys. Res.*, *96*, 20,337–20,351.

Montagner, J.-P., D.-A. Griot-Pommera, & J. Lavé (2000). How to relate body wave and surface wave anisotropy?, *J. Geophys. Res.*, *105*, 19,015–19,027.

Monteiller, V., & S. Chevrot (2011). High-resolution imaging of the deep anisotropic structure of the San Andreas Fault system beneath southern California, *Geophys. J. Int.*, *182*, 418–446.

Montési, L. G. J. (2013). Fabric development as the key for forming ductile shear zones and enabling plate tectonics, *J. Struct. Geol.*, *50*, 254–266.

Mordret, A., M. Landès, N. Shapiro, S. Singh, P. Roux, & O. Barkved (2013). Near-surface study at the Valhall oil field from ambient noise surface wave tomography, *Geophys. J. Int.*, *193*, 1627–1643.

Morris, G. B., R. W. Raitt, & G. G. Shor Jr (1969). Velocity anisotropy and delaytime maps of the mantle near Hawaii, *J. Geophys. Res.*, *74*, 4300–4316.

Moulik, P., & G. Ekström (2014). An anisotropic shear velocity model of the Earth's mantle using normal modes, body waves, surface waves and long-period waveforms, *Geophys. J. Int.*, *199*, 1713–1738.

Mühlhaus, H.-B., L. N. Moresi, B. Hobbs, & F. Dufour (2002). Large amplitude folding in finely layered viscoelastic rock structures, *Pure Appl. Geophys.*, *159*, 2311–2333.

Nagihara, S., C. R. B. Lister, & J. G. Sclater (1996). Reheating of old oceanic lithosphere: Deductions from observations, *Earth Planet. Sci. Lett.*, *139*, 91–104.

Nataf, H.-C., I. Nakanishi, & D. L. Anderson (1984). Anisotropy and shear velocity heterogeneity in the upper mantle, *Geophys. Res. Lett.*, *11*, 109–112.

Nataf, H.-C., I. Nakanishi, & D. L. Anderson (1986). Measurements of mantle wave velocities and inversion for lateral heterogeneities and anisotropy. Part III. Inversion, *J. Geophys. Res.*, *91*, 7261–7307.

Natarov, S. I., & C. P. Conrad (2012). The role of Poiseuille flow in creating depth-variation of asthenospheric shear, *Geophys. J. Int.*, *190*, 1297–1310.

Nettles, M., & A. M. Dziewoński (2008). Radially anisotropic shear-velocity structure of the upper mantle globally and beneath North America, *J. Geophys. Res.*, *113*(B02303). doi:10.1029/2006JB004819.

Nicolas, A., & N. I. Christensen (1987). Formation of anisotropy in upper mantle peridotites; a review, in *Composition, structure and dynamics of the lithosphere-asthenosphere system, Geodynamics*, vol. *16*, edited by K. Fuchs and C. Froidevaux, pp. 111–123, American Geophysical Union, Washington DC.

Nishimura, C. E., & D. W. Forsyth (1989). The anisotropic structure of the upper mantle in the Pacific, *Geophys. J. Int.*, *96*, 203–229.

Ohira, A., S. Kodaira, Y. Nakamura, G. Fujie, R. Arai, & S. Miura (2017). Evidence for frozen melts in the mid-lithosphere detected from active-source seismic data, *Sci. Rep.*, *7*(15770). doi:10.1038/s41598-017-16047-4.

Ohuchi, T., & T. Irifune (2013). Development of A-type olivine fabric in water-rich deep upper mantle, *Earth Planet. Sci. Lett.*, *361*, 20–30.

Ohuchi, T., T. Kawazoe, Y. Nishihara, & T. Irifune (2012). Change of olivine a-axis alignment induced by water: Origin of seismic anisotropy in subduction zones, *Earth Planet. Sci. Lett.*, *317*, 111–119.

Panning, M., & B. A. Romanowicz (2006). A three-dimensional radially anisotropic model of shear velocity in the whole mantle, *Geophys. J. Int.*, *167*, 361–379.

Panning, M. P., & G. Nolet (2008). Surface wave tomography for azimuthal anisotropy in a strongly reduced parameter space, *Geophys. J. Int.*, *174*, 629–648.

Parsons, B., & J. G. Sclater (1977). An analysis of the variation of ocean floor bathymetry and heat flow with age, *J. Geophys. Res.*, *82*, 803–827.

Plomerová, J., J. Šílený, & V. Babuška (1996). Joint interpretation of upper-mantle anisotropy based on teleseismic P-travel time delays and inversion of shear-wave splitting parameters, *Phys. Earth Planet. Inter.*, *95*, 293–309.

Plomerová, J., D. Kouba, & V. Babuška (2002). Mapping the lithosphere-asthenosphere boundary through changes in surface-wave anisotropy, *Tectonophys.*, *58*, 175–185.

Podolefsky, N. S., S. Zhong, & A. K. McNamara (2004). The anisotropic and rheological structure of the oceanic upper mantle from a simple model of plate shear, *Geophys. J. Int.*, *158*, 287–296.

Priestley, K., E. Debayle, D. McKenzie, & S. Pilidou (2006). Upper mantle structure of eastern Asia from multimode surface waveform tomography, *J. Geophys. Res.*, *111*(B10304). doi:10.1029/2005JB004082.

Ravenna, M. (2018). Bayesian inversion of surface-wave data for radial and azimuthal shear-wave anisotropy and the structure and evolution of southern Africa's lithosphere, Ph.D. thesis, University College Dublin, Dublin.

Ravenna, M., S. Lebedev, J. Fullea, & J. M.-C. Adam (2018). Shear-wave velocity structure of Southern Africa's lithosphere: Variations in the thickness and composition of cratons and their effect on topography, *Geochem., Geophys*., *Geosys.*, *19*, 1499–1518, doi:10.1029/2017GC007399.

Regan, J., & D. L. Anderson (1984). Anisotropic models of the upper mantle, *Phys. Earth Planet. Inter.*, *35*, 227–263.

Ribe, N. M. (1989). Seismic anisotropy and mantle flow, *J. Geophys. Res.*, *94*, 4213–4223.

Ribe, N. M., & Y. Yu (1991). A theory for plastic deformation and textural evolution of olivine polycrystals, *J. Geophys. Res.*, *96*, 8325–8335.

Ricard, Y., & C. Vigny (1989). Mantle dynamics with induced plate tectonics, *J. Geophys. Res.*, *94*, 17,543–17,559.

Ricard, Y., C. Doglioni, & R. Sabadini (1991). Differential rotation between lithosphere and mantle: A consequence of lateral mantle viscosity variations, *J. Geophys. Res.*, *96*, 8407–8415.

Richards, M., & B. H. Hager (1984). Geoid anomalies in a dynamic Earth, *J. Geophys. Res.*, *89*, 5987–6002.

Richards, M. A., & A. Lenardic (2018). The Cathles parameter (Ct): A geodynamic definition of the asthenosphere and implications for the nature of plate tectonics, *Geochem., Geophys*., *Geosys.*, *19*, 4858–4875, doi:10.1029/2018GC007664.

Ritzwoller, M. H., N. M. Shapiro, & S. Zhong (2004). Cooling history of the Pacific lithosphere, *Earth Planet. Sci. Lett.*, *226*, 69–84.

Romanowicz, B. A., & R. Snieder (1988). A new formalism for the effect of lateral heterogeneity on normal modes and surface waves. II. General anisotropic perturbation, *Geophys. J.*, *93*, 91–99.

Romanowicz, B. A., & H.-R. Wenk (2017). Anisotropy in the deep Earth, *Phys. Earth Planet. Inter.*, *269*, 58–90.

Romanowicz, B. A., & H. Yuan (2012). On the interpretation of SKS splitting measurements in the presence of several layers of anisotropy, *Geophys. J. Int.*, *188*, 1129–1140.

Rümpker, G., & P. G. Silver (1998). Apparent shear-wave splitting parameters in the presence of vertically varying anisotropy, *Geophys. J. Int.*, *135*, 790–800.

Russell, J. B., J. B. Gaherty, P.-Y. P. Lin, D. Lizarralde, J. A. Collins, G. Hirth, & R. L. Evans (2019). High-resolution constraints on Pacific upper mantle petrofabric inferred from surface-wave anisotropy, *J. Geophys. Res.*, *124*, doi: 10.1029/2018JB016598.

Ryberg, T., G. Rümpker, C. Haberland, D. Stromeyer, & M. Weber (2005). Simultaneous inversion of shear wave splitting observations from seismic arrays, *J. Geophys. Res.*, *110* (B03301). 10.1029/2004JB003,303.

Rychert, C. A., & N. Harmon (2017). Constraints on the anisotropic contributions to velocity discontinuities at ~60 km depth beneath the Pacific, *Geochem., Geophys*., *Geosys.*, *18*, 2855–2871.

Sakamaki, T., A. Suzuki, E. O. an H. Terasaki, S. Urakawa, Y. Katayama, K.-I. Funakoshi, Y. Wang, J. W. Hernlund, & M. D. Ballmer (2013). Ponded melt at the boundary between the lithosphere and asthenosphere, *Nature Geosc.*, *6*, 1041–1044.

Saltzer, R. L., J. B. Gaherty, & T. H. Jordan (2000). How are vertical shear wave splitting measurements affected by variations in the orientation of azimuthal anisotropy with depth?, *Geophys. J. Int.*, *141*, 374–390.

Savage, M. K. (1999). Seismic anisotropy and mantle deformation: What have we learned from shear wave splitting?, *Rev. Geophys.*, *37*, 65–106.

Schaeffer, A., & S. Lebedev (2013). Global shear speed structure of the upper mantle and transition zone, *Geophys. J. Int.*, *194*, 417–449.

Schaeffer, A., S. Lebedev, & T. W. Becker (2016). Azimuthal seismic anisotropy in the Earth's upper mantle and the thickness of tectonic plates, *Geophys. J. Int.*, *207*, 901–933.

Schmerr, N. (2012). The Gutenberg discontinuity: Melt at the lithosphere-asthenosphere boundary, *Science*, *335*, 1480–1483.

Schulte-Pelkum, V., & K. H. Mahan (2014). A method for mapping crustal deformation and anisotropy with receiver functions and first results from USArray, *Earth Planet. Sci. Lett.*, *402*, 221–233.

Schulte-Pelkum, V., G. Masters, & P. M. Shearer (2001). Upper mantle anistropy from long-period *P* polarization, *J. Geophys. Res.*, *106*, 21,917–21,934.

Selway, K., H. Ford, & P. Kelemen (2015). The seismic mid-lithosphere discontinuity, *Earth Planet. Sci. Lett.*, *414*, 45–57.

Semple, A. G., & A. Lenardic (2018). Plug flow in the Earth's asthenosphere, *Earth Planet. Sci. Lett.*, *496*, 29–36.

Shapiro, N. M., M. H. Ritzwoller, P. Molnar, & V. Levin (2004). Thinning and flow of Tibetan crust constrained by seismic anisotropy, *Science*, *305*, 233–236.

Shapiro, N. M., M. Campillo, L. Stehly, & M. H. Ritzwoller (2005). High-resolution surface-wave tomography from ambient seismic noise, *Science*, *307*, 1615–1618.

Silver, P. G. (1996). Seismic anisotropy beneath the continents: Probing the depths of geology, *Ann. Rev. Earth Planet. Sci.*, *24*, 385–432.

Silver, P. G., & H. H. Chan (1988). Implications for continental structure and evolution from seismic anisotropy, *Nature*, *335*, 34–39.

Silver, P. G., & M. K. Savage (1994). The interpretation of shear wave splitting parameters in the presence of two anisotropic layers, *Geophys. J. Int.*, *119*, 949–963.

Skemer, P., & L. N. Hansen (2016). Inferring upper-mantle flow from seismic anisotropy: An experimental perspective, *Tectonophys.*, *668*, 1–14.

Skemer, P., J. M. Warren, & G. Hirth (2012). The influence of deformation history on the interpretation of seismic anisotropy, *Geochem., Geophys., Geosys*., doi: 10.1029/2011GC003988.

Smith, D. B., M. H. Ritzwoller, & N. M. Shapiro (2004). Stratification of anisotropy in the Pacific upper mantle, *J. Geophys. Res.*, *109*, doi:10.1029/2004JB003200.

Smith, G. P., & G. Ekström (1999). A global study of P_n anisotropy beneath continents, *J. Geophys. Res.*, *104*, 963–980.

Smith, M. L., & F. A. Dahlen (1973). The azimuthal dependence of Love and Rayleigh wave propagation in a slightly anisotropic medium, *J. Geophys. Res*., *78*, 3321–3333, correction in doi: 10.1029/JB080i014p01923.

Song, T.-R. A., & H. Kawakatsu (2012). Subduction of oceanic asthenosphere: evidence from sub-slab seismic anisotropy, *Geophys. Res. Lett.*, *39*(L17301). doi: 10.1029/2012 GL052639.

Steinberger, B., & R. J. O'Connell (1997). Changes of the Earth's rotation axis owing to advection of mantle density heterogeneities, *Nature*, *387*, 169–173.

Sundberg, M., & R. F. Cooper (2008). Crystallographic preferred orientation produced by diffusional creep of harzburgite: Effects of chemical interactions among phases during plastic flow, *J. Geophys. Res.*, *113*(B12208). doi:10.1029/2008JB005618.

Takeo, A., K. Nishida, T. Isse, H. Kawakatsu, H. Shiobara, H. Sugioka, & T. Kanazawa (2013). Radially anisotropic structure beneath the Shikoku Basin from broadband surface wave analysis of ocean bottom seismometer records, *J. Geophys. Res.*, *118*, 2878–2892, doi:10.1002/jgrb.50219.

Takeo, A., H. Kawakatsu, T. Isse, K. Nishida, H. Shiobara, H. Sugioka, A. Ito, & H. Utada (2018). In situ characterization of the lithosphere-asthenosphere system beneath NW Pacific ocean via broadband dispersion survey with two OBS arrays, *Geochem., Geophys.*, *Geosys.*, *19*, 3529–3539, doi:10.1029/2018GC007588.

Tanimoto, T., & D. L. Anderson (1984). Mapping convection in the mantle, *Geophys. Res. Lett.*, *11*, 287–290.

Tommasi, A. (1998). Forward modeling of the development of seismic anisotropy in the upper mantle, *Earth Planet. Sci. Lett.*, *160*, 1–13.

Tommasi, A., M. Knoll, A. Vauchez, J. W. Signorelli, C. Thoraval, & R. Logé (2009). Structural reactivation in plate tectonics controlled by olivine crystals anisotropy, *Nature Geosc.*, *2*, 423–427.

Trampert, J., & H. J. van Heijst (2002). Global azimuthal anisotropy in the transition zone, *Science*, *296*, 1297–1299.

Trampert, J., & J. H. Woodhouse (2003). Global anisotropic phase velocity maps for fundamental mode surface waves between 40 and 150 s, *Geophys. J. Int.*, *154*, 154–165.

Turcotte, D. L., & E. R. Oxburgh (1967). Finite amplitude convective cells and continental drift, *J. Fluid Mech.*, *28*, 29–42.

van Hunen, J., & O. Čadek (2009). Reduced oceanic seismic anisotropy by small-scale convectin, *Earth Planet. Sci. Lett.*, *284*, 622–629.

van Summeren, J., C. P. Conrad, & C. Lithgow-Bertelloni (2012). The importance of slab pull and a global asthenosphere to plate motions, *Geochem., Geophys., Geosys.*, *13* (Q0AK03). doi:10.1029/2011GC003873.

Vine, F. J., & D. H. Matthews (1963). Magnetic anomalies over ocean ridges, *Nature*, *199*, 947–949.

Vinnik, L. P., V. Farra, & B. A. Romanowicz (1989). Azimuthal anisotropy in the Earth from observations of *SKS* at Geoscope and Nars broadband stations, *Bull. Seismol. Soc. Am.*, *79*, 1542–1558.

Vinnik, L. P., L. I. Makeyeva, A. Milev, & Y. Usenko (1992). Global patterns of azimuthal anisotropy and deformation in the continental mantle, *Geophys. J. Int.*, *111*, 433–447.

Visser, K., J. Trampert, & B. L. N. Kennett (2008). Global anisotropic phase velocity maps for higher mode Love and Rayleigh waves, *Geophys. J. Int.*, *172*, 1016–1032.

Walker, K. T., G. H. R. Bokelmann, S. L. Klemperer, & A. Nyblade (2005). Shear-wave splitting around hotspots: Evidence for upwelling-related mantle flow?, in *Plates, Plumes, and Paradigms, Geolog. Soc. Amer. Spec. Pap.*, vol. *388*, edited by G. Foulger, J. H. Natland, D. C. Presnall, & D. L. Anderson, pp. 171–192, Geological Society of America.

Wang, J., & D. Zhao (2008). P-wave anisotropic tomography beneath Northeast Japan, *Phys. Earth Planet. Inter.*, *170*, 115–133.

Wang, N., J.-P. Montagner, A. Fichtner, & Y. Capdeville (2013). Intrinsic versus extrinsic seismic anisotropy: The radial anisotropy in reference Earth models, *Geophys. Res. Lett.*, *40*, 4284–4288.

Wenk, H.-R., & C. N. Tomé (1999). Modeling dynamic recrystallization of olivine aggregates deformed in simple shear, *J. Geophys. Res.*, *104*, 25,513–25,527.

Wessel, P., & W. H. F. Smith (1998). New, improved version of the Generic Mapping Tools released, *Eos Trans. AGU*, *79*, 579.

Wookey, J., & J.-M. Kendall (2004). Evidence of midmantle anisotropy from shear wave splitting and the influence of shear-coupled P waves, *J. Geophys. Res.*, *109*, doi:10.1029/2003JB002871.

Wüstefeld, A., G. H. R. Bokelmann, G. Barruol, & J.-P. Montagner (2009). Identifying global seismic anisotropy patterns by correlating shear-wave splitting and surface-wave data, *Phys. Earth Planet. Inter.*, *176*, 198–212, available online at www.gm.univ-montp2.fr/splitting/DB/, accessed 01/2019.

Xie, J., M. H. Ritzwoller, S. Brownlee, & B. Hacker (2015). Inferring the oriented elastic tensor from surface wave observations: preliminary application across the western United States, *Geophys. J. Int.*, *201*, 996–1021.

Yuan, H., & B. A. Romanowicz (2010). Lithospheric layering in the North American continent, *Nature*, *466*, 1063–1069.

Yuan, H., B. A. Romanowicz, K. M. Fischer, & D. Abt (2011). 3-D shear wave radially and azimuthally anisotropic velocity model of the North American upper mantle, *Geophys. J. Int.*, *184*, 1237–1260.

Yuan, K., & C. Beghein (2013). Seismic anisotropy changes across upper mantle phase transitions, *Earth Planet. Sci. Lett.*, *374*, 132–144.

Zandt, G., & E. Humphreys (2008). Toroidal mantle flow through the western U.S. slab window, *Geology*, *36*, 295–298.

Zhang, S., & S.-i. Karato (1995). Lattice preferred orientation of olivine aggregates deformed in simple shear, *Nature*, *375*, 774–777.

Zhong, S. (2001). Role of ocean-continent contrast and continental keels on plate motion, net rotation of lithosphere, & the geoid, *J. Geophys. Res.*, *106*, 703–712.

Zhou, Q., J. S. Hu, L. J. Liu, T. Chaparro, D. Stegman, & M. Faccenda (2018). Western US seismic anisotropy revealing complex mantle dynamics, *Earth Planet. Sci. Lett.*, *500*, 156–167.